The Astrophysical Journal, 869:113 (15pp), 2018 December 20 https://doi.org/10.3847/1538-4357/aae820

Black Hole Mass Scaling Relations for Spiral Galaxies. II. $M_{\rm BH}$–$M_{*,\rm tot}$ and $M_{\rm BH}$–$M_{*,\rm disk}$

Benjamin L. Davis[1], Alister W. Graham[1], and Ewan Cameron[2]
[1] Centre for Astrophysics and Supercomputing, Swinburne University of Technology, Hawthorn, Victoria 3122, Australia; benjamindavis@swin.edu.au
[2] Oxford Big Data Institute, University of Oxford, Oxford OX3 7LF, UK
Received 2018 May 22; revised 2018 October 8; accepted 2018 October 10; published 2018 December 17

Abstract

Black hole mass ($M_{\rm BH}$) scaling relations are typically derived using the properties of a galaxy's bulge and samples dominated by (high-mass) early-type galaxies. Studying late-type galaxies should provide greater insight into the mutual growth of black holes and galaxies in more gas-rich environments. We have used 40 spiral galaxies to establish how $M_{\rm BH}$ scales with both the total stellar mass ($M_{*,\rm tot}$) and the disk's stellar mass, having measured the spheroid (bulge) stellar mass ($M_{*,\rm sph}$) and presented the $M_{\rm BH}$–$M_{*,\rm sph}$ relation in Paper I. The relation involving $M_{*,\rm tot}$ may be beneficial for estimating $M_{\rm BH}$ either from pipeline data or at higher redshift, conditions that are not ideal for the accurate isolation of the bulge. A symmetric Bayesian analysis finds $\log(M_{\rm BH}/{\rm M}_{\odot}) = (3.05^{+0.57}_{-0.49})\log\{M_{*,\rm tot}/[\upsilon(6.37\times10^{10}\,M_{\odot})]\} + (7.25^{+0.13}_{-0.14})$. The scatter from the regression of $M_{\rm BH}$ on $M_{*,\rm tot}$ is 0.66 dex; compare 0.56 dex for $M_{\rm BH}$ on $M_{*,\rm sph}$ and 0.57 dex for $M_{\rm BH}$ on σ_*. The slope is >2 times that obtained using core-Sérsic early-type galaxies, echoing a similar result involving $M_{*,\rm sph}$, and supporting a varied growth mechanism among different morphological types. This steeper relation has consequences for galaxy/black hole formation theories, simulations, and predicting black hole masses. We caution that (i) an $M_{\rm BH}$–$M_{*,\rm tot}$ relation built from a mixture of early- and late-type galaxies will find an arbitrary slope of approximately 1–3, with no physical meaning beyond one's sample selection, and (ii) evolutionary studies of the $M_{\rm BH}$–$M_{*,\rm tot}$ relation need to be mindful of the galaxy types included at each epoch. We additionally update the $M_{*,\rm tot}$–(*face-on* spiral arm pitch angle) relation.

Key words: black hole physics – galaxies: bulges – galaxies: evolution – galaxies: fundamental parameters – galaxies: spiral – galaxies: structure

1. Introduction

Davis et al. (2018, hereafter Paper I) illustrate that the accurate measurement of a galaxy's bulge (spheroid)[3] luminosity is a time-consuming task requiring a considerable level of care. The difficulty lies in the need to correctly decompose the surface brightness maps or light profiles of galaxies into their constituent components, whereas the task of just summing up all the light in a galaxy to obtain its total luminosity is a comparatively simple process. Nonetheless, for some two decades astronomers have attempted this decomposition because the centrally located supermassive black hole (SMBH) mass ($M_{\rm BH}$) is thought to correlate with the properties of the bulge (Dressler 1989). However, the existence of supermassive black holes in bulgeless galaxies (Paper I, and references therein) reveals that there is more to it than this.

It is a small mystery why the $M_{\rm BH}$–$M_{*,\rm tot}$ (black hole mass to total galaxy stellar mass) relation has not been explored further in the literature. To date, its limited publication history has not been without dramatic disagreement. The very existence of an $M_{\rm BH}$–$M_{*,\rm tot}$ relation (or its proxy relation with bulge luminosity) has improved infinitely from a state of nonexistence (Kormendy & Gebhardt 2001) to existing, but not being as strong a tracer of supermassive black hole mass as the bulge (Beifiori et al. 2012; Savorgnan et al. 2016), to being elevated to a stature equal with that of the bulge (Läsker et al. 2014; Mutlu-Pakdil et al. 2018). The latter claim would bring the $M_{\rm BH}$–$M_{*,\rm tot}$ relation in line with suggestions that SMBH growth is a derivative of the overall potential of its host galaxy (Ferrarese 2002; Volonteri et al. 2011). Part of the explanation to this small mystery undoubtedly pertains to the bend in the $M_{\rm BH}$–$M_{*,\rm sph}$ (black hole mass to spheroid stellar mass) relation (Graham 2012; Graham & Scott 2013; Scott et al. 2013), which steepens at the low-mass end, departing from the near-linear relation defined by massive early-type galaxies. Given the departure of these low-mass bulges from the original near-linear $M_{\rm BH}$–$M_{*,\rm sph}$ relation, the use of total galaxy mass would have resulted in even greater departures and perhaps the belief that black hole mass does not correlate with galaxy mass (see Graham 2016 for a review of black hole scaling relations).

The need for an $M_{\rm BH}$–$M_{*,\rm tot}$ relation becomes more critical for nonlocal galaxies. At higher redshifts, the difficultly of accurately separating the bulge light from the remaining light of a galaxy becomes increasingly perilous, due to the reduced spatial resolution. In the past decade, this connection has been widely studied (e.g., Merloni et al. 2010; Bennert et al. 2011; Cisternas et al. 2011; Yang et al. 2018), with some investigations of nonlocal galaxies going as far as to say that the $M_{\rm BH}$–$M_{*,\rm tot}$ relation is correlated as tightly as, or tighter than, the $M_{\rm BH}$–$M_{*,\rm sph}$ relation (Peng 2007; Jahnke et al. 2009; Bennert et al. 2010). In light of this, our endeavor to focus on the $M_{\rm BH}$–$M_{*,\rm tot}$ relation in local spiral galaxies with directly measured SMBH masses will serve as a useful benchmark for studies of galaxies at higher redshifts, including evolutionary studies (e.g., Labbé et al. 2003; Kollmeier et al. 2006; Hopkins et al. 2008; Walter et al. 2016; Burkert et al. 2016; Contini et al. 2016; Yuan et al. 2017). This should allow for an enrichment in our knowledge of the star formation history (e.g., Shankar et al. 2009) and dry merger history (e.g., Jahnke & Macciò 2011) of SMBH host galaxies.

The necessity for improving our knowledge of the $M_{\rm BH}$–$M_{*,\rm tot}$ relation becomes even more manifest in the lofty goals and pragmatism surrounding large surveys of galaxies. Due to time

[3] We use the terms "spheroid" and "bulge" interchangeably.

requirements, studies of even as few as $\approx 10^2$ galaxies must rely on *automated* bulge/disk decompositions out of necessity. Even if the $M_{\rm BH}$–$M_{*,\rm sph}$ relation were intrinsically more accurate than the $M_{\rm BH}$–$M_{*,\rm tot}$ relation, the benefits of less intrinsic scatter in the $M_{\rm BH}$–$M_{*,\rm sph}$ relation might be overcome by the inherent measurement errors associated with bulge/disk decompositions produced via pipeline software. At our current technological limits, there likely exists a ceiling in terms of survey size or redshift, beyond which the $M_{\rm BH}$–$M_{*,\rm tot}$ relation is of greater benefit than the $M_{\rm BH}$–$M_{*,\rm sph}$ relation.

Furthermore, as discussed in Davis et al. (2017) and Paper I, pseudobulges have been slandered as being pariahs and proverbial black sheep in the family of black hole mass scaling relations. Despite one's personal opinions concerning pseudobulges and their role in complementing/hindering studies of the $M_{\rm BH}$–$M_{*,\rm sph}$ relation, substitution with the $M_{\rm BH}$–$M_{*,\rm tot}$ relation allows one to seemingly escape from the stigma surrounding pseudobulges. Moreover, if galaxies with pseudobulges participate in the $M_{\rm BH}$–$M_{*,\rm tot}$ relation, as they do in the $M_{\rm BH}$–$M_{*,\rm sph}$ relation (Paper I), this may suggest that a relation also exists with the disk stellar mass ($M_{*,\rm disk}$). This is especially true in the case of low-mass, disk-dominated spiral galaxies with pseudobulges as a result of the secular evolution of their galactic disk (Combes & Sanders 1981; Combes 2009, 2017). Therefore, examining the existence of an $M_{\rm BH}$–$M_{*,\rm disk}$ relation will be a secondary goal of this paper, behind our primary goal of exploring the $M_{\rm BH}$–$M_{*,\rm tot}$ relation.

Our measurement of the disk stellar masses depends on the (rather meticulous) multicomponent galaxy decompositions presented in Paper I. In addition to modeling the disk, bulge, and bar (when present), rings, spiral arms, and additional nuclear components were also accounted for, as these can otherwise bias the Sérsic bulge parameters.

In the following section, we will briefly recapitulate the sample selection and the light profile analysis as performed in Paper I, before touching on newer complements from studying the whole of the individual galaxies. In Section 3, we compare our galaxy apparent magnitudes with similar studies in the literature. In Section 4, we have applied a sophisticated Bayesian analysis to obtain the optimal $M_{\rm BH}$–$M_{*,\rm tot}$ (and $M_{\rm BH}$–$M_{*,\rm disk}$) scaling relation for spiral galaxies, which could be highly useful, if the scatter is acceptably low, because it does not require bulge/disk/etc. decompositions. We have also included the results using the more familiar BCES linear regression from Akritas & Bershady (1996) and the modified FITEXY routine (Press et al. 1992; Tremaine et al. 2002). Finally, given that the spiral arm pitch angle (ϕ) traces the black hole mass (Seigar et al. 2008; Berrier et al. 2013; Davis et al. 2017), we have additionally explored the complementary relationships between $M_{*,\rm tot}$ and ϕ and between $M_{*,\rm disk}$ and ϕ, checking for consistency and insight. We provide a discussion of our results in Section 5 and explore how these relations will aid in the prediction of black hole masses, particularly intermediate-mass black holes (IMBHs). Finally, we summarize the overall outcomes of this paper in Section 6. In the appendices, we provide useful error propagation formulae (Appendix A) and the priors and posterior values from our Bayesian regressions (Appendix B).

Unless noted otherwise, all printed errors and plotted error bars represent 1σ ($\approx$68.3%) confidence levels. Magnitudes are expressed in the absolute (AB) system (Oke 1974).

2. Data and Methodology

Davis et al. (2017) presented what we believe was, at the time, the complete sample of spiral galaxies with directly measured SMBH masses. A contemporary analysis of astrophysical publications had revealed 44 *spiral* galaxies whose central SMBH masses had been measured via proper motion, stellar dynamics, gaseous dynamics, and/or astrophysical maser emission.[4] This remains the largest such spiral galaxy sample published to date, and references to the publications that determined the black hole masses (listed here in Table 1 for convenience) have been provided in Davis et al. (2017). The original sample of 44 galaxies has been culled to 40 spiral galaxies with spheroids after the removal of Cygnus A (an early-type galaxy with a spiral in its intermediate-scale disk) and three bulgeless galaxies. Although the three bulgeless galaxies (NGC 2478, NGC 4395, and NGC 6926) could be included in our study of the $M_{\rm BH}$–$M_{*,\rm tot}$ and $M_{\rm BH}$–$M_{*,\rm disk}$ relations, we will use the same sample of 40 galaxies as in Paper I, as this will enable a cleaner comparison of the black hole mass scaling relations for spiral galaxies. In particular, there is the question of how much scatter there is about the $M_{\rm BH}$–$M_{*,\rm sph}$ relation versus the $M_{\rm BH}$–$M_{*,\rm tot}$ relation.

Our imaging data consist primarily of *Spitzer Space Telescope* 3.6 μm imaging from the *Spitzer* Survey of Stellar Structure in Galaxies (S^{4}G; Sheth et al. 2010), supplemented with *Hubble Space Telescope* F814W and Two Micron All Sky Survey (2MASS) K_s-band (2.2 μm) imaging. Isophotal fitting was performed using the software routines ISOFIT and CMODEL (Ciambur 2015). The original images were first sky-subtracted and carefully masked for contaminating foreground and background sources, and the galaxy light was then measured with a concentric set of quasi-elliptical isophotes whose geometries were defined by their eccentric anomalies—this allows for an accurate modeling of the light distribution via the inclusion of Fourier harmonic terms that capture deviations from pure elliptical isophotes. The associated 1D surface brightness profiles were then matched to models, which had been convolved with the image-dependent point-spread function (PSF).

Galaxies were carefully decomposed into multiple components, accounting for bulges, disks, bars, point sources, rings, and spiral arms, when present, using the PROFILER software (Ciambur 2016). Decompositions for every galaxy can be seen in Paper I. Components were identified not only based on their appearance in the 2D image (viewed at a range of contrasts) but also using the ellipticity profile, the position angle profile, the B_4 Fourier harmonic profile that captures the boxy or disky nature of the isophotes, and of course the surface brightness profile. Rather than adding arbitrary Sérsic components until some minimum χ^2 value is reached—a practice seen in the literature of late—we only include a component if we can clearly identify it with a specific physical entity, such as a bar or a ring. Paper I lists which filter was used for each galaxy and shows the galaxy decomposition.

2.1. Magnitudes and Stellar Masses

The apparent and absolute magnitudes of the spheroids are listed in Table 3 of Paper I. Here we tabulate the total *galaxy* apparent magnitudes (m), determined within the PROFILER

[4] We have not detected any offsets in the spiral galaxy scaling relations based on the method used to measure the black hole mass.

Table 1
Galaxy Sample and Masses

Galaxy Name	Type	λ (μm)	A_λ (mag)	$\log(M_{\rm BH}/M_\odot)$	$\lvert\phi\rvert$ (deg)	$m_{\lambda,\rm tot}$ (mag)	$\mathfrak{M}_{\lambda,\rm tot}$ (mag)	$\log(M_{*,\rm tot}/M_\odot)$	$\log(M_{*,\rm disk}/M_\odot)$	B/T
(1)	(2)	(3)	(4)	(5)	(6)	(7)	(8)	(9)	(10)	(11)
Circinus	3.3 ± 1.2[a]	3.550	0.265	$6.25^{+0.10}_{-0.12}$	17.0 ± 3.9	7.00 ± 0.11	-21.09 ± 0.41	10.62 ± 0.18	10.46 ± 0.19	0.31 ± 0.09
Cygnus A	5.0 ± 2.0	0.8012	0.067	$9.44^{+0.11}_{-0.14}$	2.7 ± 0.2	12.22 ± 0.43	-25.74 ± 0.43	12.38 ± 0.20	11.04 ± 5.33	0.95 ± 0.55
ESO558-G009	3.9 ± 2.1	0.8024	0.610	$7.26^{+0.03}_{-0.04}$	16.5 ± 1.3	13.70 ± 0.05	-22.36 ± 0.06	11.03 ± 0.10	10.99 ± 0.10	0.07 ± 0.01
IC 2560	3.4 ± 0.6[a]	3.550	0.017	$6.49^{+0.19}_{-0.21}$	22.4 ± 1.7	11.03 ± 0.08	-21.18 ± 0.92	10.66 ± 0.37	10.61 ± 0.37	0.09 ± 0.03
J0437+2456[b]	…[a]	0.8024	1.821	$6.51^{+0.04}_{-0.05}$	16.9 ± 4.1	14.00 ± 0.05	-22.22 ± 0.06	10.97 ± 0.10	10.93 ± 0.12	0.09 ± 0.04
Milky Way	…[a]	0.7625	…	6.60 ± 0.02	13.1 ± 0.6	…	-21.25 ± 0.05[c]	10.78 ± 0.10[d]	10.71 ± 0.11[d]	0.15 ± 0.02[d]
Mrk 1029	…	0.8024	0.064	$6.33^{+0.10}_{-0.13}$	17.9 ± 2.1	14.47 ± 0.04	-21.44 ± 0.05	10.66 ± 0.09	10.57 ± 0.10	0.18 ± 0.02
NGC 0224	3.0 ± 0.4[a]	3.550	0.124	$8.15^{+0.22}_{-0.11}$	8.5 ± 1.3	2.45 ± 0.15[e]	-21.75 ± 0.17[f]	10.88 ± 0.10[f]	10.81 ± 0.10	0.17 ± 0.03
NGC 0253	5.1 ± 0.4[a]	3.550	0.003	7.00 ± 0.30	13.8 ± 2.3	6.08 ± 0.05	-21.32 ± 0.11	10.71 ± 0.08	10.66 ± 0.08	0.11 ± 0.01
NGC 1068	3.0 ± 0.3[a]	2.159	0.010	6.75 ± 0.08	17.3 ± 1.9	7.64 ± 0.18	-22.39 ± 0.43	10.78 ± 0.18	10.62 ± 0.21	0.31 ± 0.13
NGC 1097	3.3 ± 0.5[a]	3.550	0.005	$8.38^{+0.03}_{-0.04}$	9.5 ± 1.3	8.65 ± 0.14	-23.05 ± 0.18	11.40 ± 0.10	11.27 ± 0.13	0.27 ± 0.12
NGC 1300	4.0 ± 0.2[a]	3.550	0.005	$7.71^{+0.19}_{-0.14}$	12.7 ± 2.0	10.25 ± 0.09	-20.28 ± 0.39	10.30 ± 0.17	10.24 ± 0.17	0.13 ± 0.06
NGC 1320	0.9 ± 0.9	3.550	0.008	$6.78^{+0.24}_{-0.34}$	19.3 ± 2.0	11.63 ± 0.10	-20.99 ± 0.97	10.58 ± 0.40	10.30 ± 0.41	0.47 ± 0.09
NGC 1398	2.0 ± 0.3[a]	3.550	0.002	8.03 ± 0.11	9.7 ± 0.7	9.03 ± 0.10	-22.65 ± 0.41	11.25 ± 0.18	11.14 ± 0.18	0.21 ± 0.05
NGC 2273	0.9 ± 0.4[a]	0.8024	0.107	6.97 ± 0.09	15.2 ± 3.9	10.91 ± 0.04	-21.72 ± 0.43	10.77 ± 0.19	10.69 ± 0.20	0.16 ± 0.02
NGC 2748	4.0 ± 0.1	0.8012	0.041	$7.54^{+0.17}_{-0.25}$	6.8 ± 2.2	11.34 ± 0.10	-20.02 ± 0.51	10.09 ± 0.22	10.09 ± 0.22	…
NGC 2960	0.8 ± 0.9	3.550	0.008	$7.06^{+0.16}_{-0.17}$	14.9 ± 1.9	12.34 ± 0.12	-21.68 ± 0.83	10.86 ± 0.34	10.65 ± 0.35	0.38 ± 0.11
NGC 2974	…[a]	3.550	0.010	$8.23^{+0.07}_{-0.08}$	10.5 ± 2.9	10.03 ± 0.05	-21.36 ± 0.27	10.73 ± 0.12	10.56 ± 0.13	0.32 ± 0.04
NGC 3031	2.4 ± 0.6[a]	3.550	0.014	$7.83^{+0.11}_{-0.07}$	13.4 ± 2.3	6.27 ± 0.07	-21.15 ± 0.12	10.65 ± 0.08	10.47 ± 0.10	0.33 ± 0.06
NGC 3079	6.4 ± 1.1[a]	3.550	0.002	$6.38^{+0.11}_{-0.13}$	20.6 ± 3.8	9.56 ± 0.20	-21.24 ± 0.43	10.68 ± 0.18	10.60 ± 0.20	0.17 ± 0.08
NGC 3227	1.5 ± 0.9[a]	3.550	0.004	$7.88^{+0.13}_{-0.14}$	7.7 ± 1.4	9.79 ± 0.06	-21.54 ± 0.32	10.80 ± 0.14	10.72 ± 0.15	0.17 ± 0.04
NGC 3368	2.1 ± 0.7[a]	3.550	0.004	$6.89^{+0.08}_{-0.10}$	14.0 ± 1.4	8.61 ± 0.03	-21.25 ± 0.14	10.69 ± 0.09	10.63 ± 0.09	0.13 ± 0.02
NGC 3393	1.2 ± 0.7[a]	0.8024	0.116	$7.49^{+0.05}_{-0.16}$	13.1 ± 2.5	11.62 ± 0.09	-22.30 ± 0.10	11.00 ± 0.10	10.92 ± 0.10	0.17 ± 0.03
NGC 3627	3.1 ± 0.4[a]	3.550	0.006	6.95 ± 0.05	18.6 ± 2.9	8.35 ± 0.11	-21.48 ± 0.18	10.78 ± 0.10	10.73 ± 0.10	0.09 ± 0.04
NGC 4151	1.9 ± 0.5[a]	3.550	0.005	$7.68^{+0.15}_{-0.58}$	11.8 ± 1.8	10.02 ± 0.10	-21.09 ± 0.31	10.62 ± 0.14	10.36 ± 0.16	0.45 ± 0.08
NGC 4258	4.0 ± 0.2[a]	3.550	0.003	7.60 ± 0.01	13.2 ± 2.5	7.76 ± 0.12	-21.34 ± 0.14	10.72 ± 0.09	10.62 ± 0.10	0.21 ± 0.09
NGC 4303	4.0 ± 0.1[a]	3.550	0.004	$6.58^{+0.07}_{-0.26}$	14.7 ± 0.9	9.45 ± 0.10	-20.72 ± 0.15	10.48 ± 0.09	10.44 ± 0.09	0.09 ± 0.01
NGC 4388	2.8 ± 0.7[a]	3.550	0.006	6.90 ± 0.11	18.6 ± 2.6	10.35 ± 0.15	-20.63 ± 0.53	10.44 ± 0.22	10.20 ± 0.24	0.42 ± 0.08
NGC 4395	8.8 ± 0.5[a]	3.550	0.003	$5.64^{+0.22}_{-0.12}$	22.7 ± 3.6	9.93 ± 0.11	-18.16 ± 0.12	9.45 ± 0.08	9.45 ± 0.08	…
NGC 4501	3.3 ± 0.6	3.550	0.007	7.13 ± 0.08	12.2 ± 3.4	8.76 ± 0.11	-21.21 ± 0.12	10.67 ± 0.08	10.53 ± 0.11	0.28 ± 0.10
NGC 4594	1.1 ± 0.4	3.550	0.009	8.34 ± 0.10	5.2 ± 0.4	7.51 ± 0.28	-22.11 ± 0.31	11.03 ± 0.14	10.63 ± 0.40	0.60 ± 0.30
NGC 4699	2.9 ± 0.4[a]	3.550	0.006	$8.34^{+0.13}_{-0.15}$	5.1 ± 0.4	8.84 ± 0.31	-22.75 ± 0.54	11.29 ± 0.23	10.79 ± 0.58	0.68 ± 0.34
NGC 4736	2.3 ± 0.8[a]	3.550	0.003	$6.78^{+0.09}_{-0.11}$	15.0 ± 2.3	7.47 ± 0.08	-20.45 ± 0.11	10.37 ± 0.08	10.19 ± 0.09	0.33 ± 0.05
NGC 4826	2.2 ± 0.6	3.550	0.007	$6.07^{+0.14}_{-0.16}$	24.3 ± 1.5	7.86 ± 0.04	-20.56 ± 0.51	10.41 ± 0.21	10.35 ± 0.21	0.14 ± 0.02
NGC 4945	6.1 ± 0.6[a]	2.159	0.055	6.15 ± 0.30	22.2 ± 3.0	6.18 ± 0.13	-21.73 ± 0.17	10.52 ± 0.09	10.48 ± 0.09	0.07 ± 0.03
NGC 5055	4.0 ± 0.2	3.550	0.003	$8.94^{+0.09}_{-0.11}$	4.1 ± 0.4	7.89 ± 0.14	-21.55 ± 0.18	10.81 ± 0.10	10.52 ± 0.15	0.48 ± 0.10
NGC 5495	5.0 ± 0.4[a]	0.8024	0.089	$7.04^{+0.08}_{-0.09}$	13.3 ± 1.4	12.15 ± 0.07	-23.08 ± 0.07	11.31 ± 0.10	11.23 ± 0.10	0.17 ± 0.03
NGC 5765b	2.8 ± 1.5[a]	0.8024	0.057	7.72 ± 0.05	13.5 ± 3.9	13.26 ± 0.04	-22.57 ± 0.19	11.11 ± 0.12	11.07 ± 0.12	0.08 ± 0.01
NGC 6264	2.7 ± 1.3[a]	0.8024	0.100	7.51 ± 0.06	7.5 ± 2.7	13.79 ± 0.03	-22.45 ± 0.27	11.06 ± 0.14	11.02 ± 0.14	0.09 ± 0.01
NGC 6323	2.0 ± 0.3[a]	0.8024	0.026	$7.02^{+0.13}_{-0.14}$	11.2 ± 1.3	13.11 ± 0.04	-22.40 ± 0.67	11.04 ± 0.28	11.01 ± 0.28	0.07 ± 0.02
NGC 6926	5.6 ± 2.3[a]	3.550	0.029	$7.74^{+0.26}_{-0.74}$	9.1 ± 0.7	11.71 ± 0.07	-22.80 ± 0.12	11.31 ± 0.08	11.31 ± 0.08	…

Table 1
(Continued)

Galaxy Name	Type	λ (μm)	A_λ (mag)	$\log(M_{\rm BH}/M_\odot)$	$\lvert\phi\rvert$ (deg)	$\mathfrak{m}_{\lambda,\rm tot}$ (mag)	$\mathfrak{M}_{\lambda,\rm tot}$ (mag)	$\log(M_{*,\rm tot}/M_\odot)$	$\log(M_{*,\rm disk}/M_\odot)$	B/T
(1)	(2)	(3)	(4)	(5)	(6)	(7)	(8)	(9)	(10)	(11)
NGC 7582	2.1 ± 0.5[a]	3.550	0.002	$7.67^{+0.09}_{-0.08}$	10.9 ± 1.6	9.74 ± 0.18	-21.47 ± 0.21	10.77 ± 0.11	10.65 ± 0.14	0.24 ± 0.11
UGC 3789	1.6 ± 0.6[a]	0.8024	0.100	7.06 ± 0.05	10.4 ± 1.9	12.00 ± 0.06	-21.64 ± 0.23	10.74 ± 0.13	10.60 ± 0.13	0.28 ± 0.04
UGC 6093	3.7 ± 0.8[a]	0.8024	0.041	$7.41^{+0.04}_{-0.03}$[g]	10.2 ± 0.9	13.23 ± 0.08	-22.94 ± 0.17	11.26 ± 0.11	11.20 ± 0.12	0.12 ± 0.02

Notes. Column (1): galaxy name. Column (2): numerical morphological type from HyperLeda. Column (3): filter wavelength (see Paper I, Table 1). Column (4): Galactic extinction (in mag) due to dust attenuation in the Milky Way, at the reference wavelength listed in Column (3), from Schlafly & Finkbeiner (2011). Column (5): black hole mass listed in Davis et al. (2017), compiled from references therein. Column (6): logarithmic spiral arm pitch angle (*face-on*, absolute value in degrees) from Davis et al. (2017). Column (7): galaxy apparent magnitude (in AB mag) for the wavelength listed in Column (3) (calculated via Paper I, Equations (4) and (5)). Column (8): fully corrected galaxy absolute magnitude (in AB mag) for the wavelength listed in Column (3) (calculated via Paper I, Equation (6)); *Spitzer* images are additionally corrected for dust emission. Column (9): total galaxy stellar mass (from the galaxy absolute magnitude in Column (8), converted to a stellar mass using the appropriate solar absolute magnitude and stellar mass-to-light ratios from Paper I, Table 1). Column (10): disk stellar mass (via Equation (2)). Column (11): bulge-to-total flux ratio.

[a] Indicates a barred morphology.
[b] SDSS J043703.67+245606.8
[c] From Okamoto (2013).
[d] From Licquia & Newman (2015).
[e] From Savorgnan & Graham (2016).
[f] From Savorgnan et al. (2016).
[g] From Zhao et al. (2018).

software by integrating the equivalent-axis[5] intensity model to obtain the apparent luminosity given by

$$L = 2\pi \int_0^{R_{\rm eq} \gg h} I\, R_{\rm eq}\, dR_{\rm eq}, \quad (1)$$

where $I \equiv I(R_{\rm eq})$ is the intensity as a function of the equivalent-axis radius ($R_{\rm eq}$), h is the scale length of the exponential disk, and $\mathfrak{m} \propto -2.5 \log L$. The (corrected)[6] total galaxy absolute magnitudes ($\mathfrak{M}$) are calculated via Equation (6) from Paper I.

As in Paper I, we account for the emission of dust at 3.6 μm wavelengths according to the study of Querejeta et al. (2015). This includes a stellar M_*/L_* ratio of 0.60 ± 0.09 from Meidt et al. (2014) and a ≈25% reduction to the observed luminosity due to dust glow. Our dust emission correction resulted in $\Delta \log(M_{*,\rm tot}/M_\odot) = -0.12$ dex for all of our 28 galaxies with 3.6 μm imaging.

We have applied stellar mass-to-light ratios (with Chabrier 2003 initial mass functions [IMFs]) and solar absolute magnitudes consistent with Table 1 in Paper I to calculate the stellar masses. As an additional check, we calculated the stellar masses using the 2MASS magnitudes and a (stellar mass)-to-(stellar light) ratio of 0.62 ± 0.08, which yielded a very good agreement.

We derive the disk stellar mass, $M_{*,\rm disk}$, via simple subtraction such that

$$M_{*,\rm disk} \equiv M_{*,\rm tot} - M_{*,\rm sph}. \quad (2)$$

This definition includes the spiral arms, rings, and bars (if present) as a part of the "disk." Errors on $\mathfrak{m}$ are estimated from the uncertainties on the intensity model and propagated, along with uncertainties on other variables (e.g., distance), when calculating $\mathfrak{M}$ and all derivative quantities (e.g., stellar mass). For a detailed list of error propagation formulae, see Appendix A. Our sample and relevant data are tabulated in Table 1.

2.2. Colors

Our sample represents all of the currently known spiral galaxies with directly measured black hole masses. However, the colors of these spiral galaxies are not representative of the full spiral galaxy population. As can be seen in Figure 1, the majority of our galaxies have colors clustered around a median $B-K$ color equal to 3.77 ± 0.22 mag, where the B-band magnitudes have come from the Third Reference Catalog of Bright Galaxies (RC3; de Vaucouleurs et al. 1991) and the K-band magnitudes have come from 2MASS.[7] Furthermore, we have corrected the magnitudes for Galactic extinction (Schlafly & Finkbeiner 2011). This galaxy selection "bias" is not unexpected though: given the necessity to resolve the gravitational sphere of influence around the black holes, only the most massive black holes can be directly measured, yielding host spiral galaxies that are more massive and redder than a general population of "blue cloud" spiral galaxies (Cassata et al. 2007). The roughly constant color gives additional support to our use of a constant stellar mass-to-light ratio in the *Spitzer* 3.6 μm band. That is, the lack of a trend between color and magnitude in our sample suggests that our galaxies' stellar masses should not simply be thought of as scaled luminosities, but indeed as stellar masses.

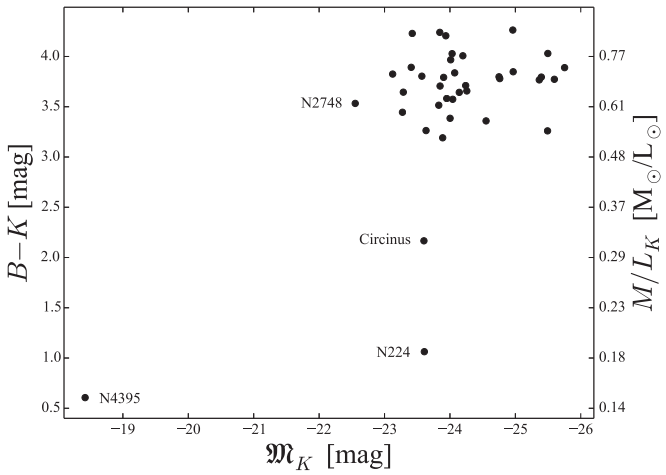

Figure 1. *B-K* color–magnitude diagram for our spiral galaxy sample. The associated *K*-band stellar mass-to-light ratios (via the prescription based on the $B-K$ color; Bell & de Jong 2001) are shown on the right axis.

While red spiral galaxies are known to have a range of morphologies (Masters et al. 2010; Chilingarian & Zolotukhin 2012), they are rare at stellar masses less than $10^{10}\,M_\odot$. One may speculate whether our spiral galaxies are red because they have black holes that are massive enough to have blown out their gas and quench their star formation. Arguably, Savorgnan et al. (2016) may, therefore, have prematurely referred to the spiral galaxy sequence in the $M_{\rm BH}$–$M_{*,\rm sph}$ diagram as a blue sequence. However, it is known that some low-mass, blue, spiral galaxies possess active galactic nuclei—for example, NGC 4395 (den Brok et al. 2015) and LEDA 87300 (Baldassare et al. 2015; Graham et al. 2016)—and therefore we are simply probing the red end of the blue sequence. LEDA 87300 has a $g'-r'$ color equal to 0.41 mag (Graham et al. 2016), which is slightly bluer than NGC 4395 with $g'-r' = 0.50$ mag.[8]

2.3. υ

In Paper I, we introduced a new parameter,[9] υ It is our hope that readers may easily apply the scaling relations herein to their own studies by calibrating to their adopted initial mass function. This conversion is accomplished in a fashion similar to that achieved via h in cosmological conversions. Often, cosmologists will normalize their cosmologies, where $h = 1$ implies a Hubble constant of 100 km s^{-1} Mpc^{-1}. Similarly, researchers who conduct simulations of galaxies will often normalize their initial-mass-function-dependent stellar mass-to-light ratio, Υ_*.

For example, from 40 of our 43 galaxies with available photometry on NED,[10] we find that $\upsilon = 1.08 \pm 0.15$ when comparing our galaxy stellar masses (Table 1) to those predicted using 2MASS K-band magnitudes and the $B-K$ color-dependent stellar mass-to-light ratios from Bell & de Jong (2001).

[5] Defined by the geometric mean $\sqrt{ab}$, where a and b are the major- and minor-axis lengths of a given isophote, respectively; the "equivalent axis" can be considered equivalent to a circle of the same radius.

[6] We corrected for Galactic extinction, cosmological redshift dimming, and K-corrections, in addition to dust (see Paper I).

[7] http://www.ipac.caltech.edu/2mass, Jarrett et al. (2000).

[8] Here, the magnitudes are obtained from the Sloan Digital Sky Survey Data Release 6 (http://www.sdss.org/dr6/products/catalogs/index.html) and subsequently corrected for Galactic extinction (Schlafly & Finkbeiner 2011).

[9] The value of υ has no affect on the slope of the scaling relations.

[10] http://nedwww.ipac.caltech.edu

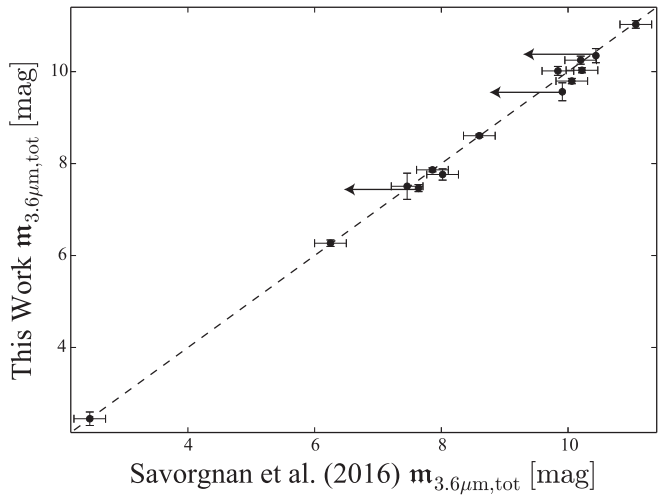

Figure 2. Comparison of the total 3.6 μm apparent magnitudes (with a 1:1 dashed line) from 14 spiral galaxies in common with Savorgnan & Graham (2016) yields $\Delta_{rms,\perp} = 0.07$ mag. Three of the values from Savorgnan & Graham (2016) are upper limits, indicated with arrows. Note that the Vega magnitudes from Savorgnan & Graham (2016) have been converted here to the AB magnitude system.

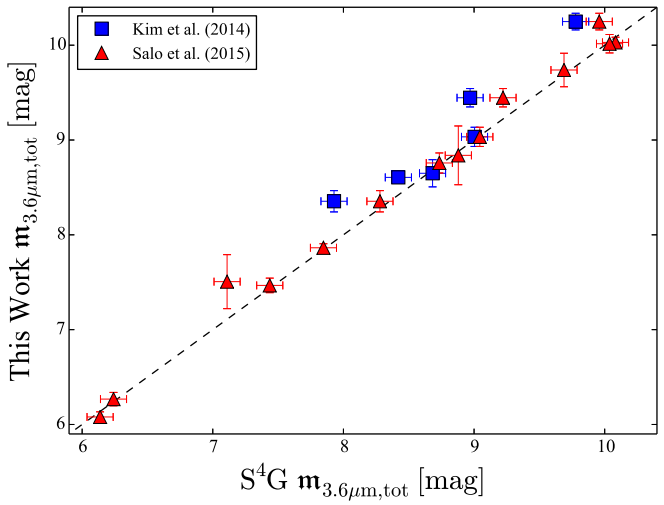

Figure 3. Comparison of the total 3.6 μm apparent magnitudes (with 1:1 dashed line) for data from 14 spiral galaxies that are in common with the S^{4}G sample from Salo et al. (2015) plus six from Kim et al. (2014). The agreement is such that $\Delta_{rms,\perp} = 0.09$ mag (Kim et al. 2014) and $\Delta_{rms,\perp} = 0.06$ mag (Salo et al. 2015). Note that the S^{4}G does not provide error estimates, so we have added error bars equivalent to our median error.

Alternatively, to adjust our stellar masses to match those predicted from the Sloan Digital Sky Survey (SDSS) i'-band magnitudes and $g' - i'$ color-dependent stellar mass-to-light ratios from Bell et al. (2003), Taylor et al. (2011), or Roediger & Courteau (2015) would require $\upsilon = 0.81 \pm 0.17$, 0.36 ± 0.09, or 0.51 ± 0.10, respectively.

3. Comparison of 3.6 μm Magnitudes

3.1. Savorgnan & Graham (2016)

We first compare our data set with that of Savorgnan & Graham (2016). Our work builds on those studies by analyzing many of the same galaxies, in the same 3.6 μm passband, and with similar decompositional methodology. Figure 2 shows that our total apparent magnitudes match well with Savorgnan et al. (2016), with an rms scatter $\Delta_{rms,\perp} = 0.07$ mag.[11] We find this high level of agreement to be four times tighter than between the spheroid apparent magnitudes for the same galaxies, reflective of the challenges in obtaining bulge magnitudes.

The multicomponent surface brightness profile decompositional methodology of Savorgnan & Graham (2016) largely agrees with ours. Both methods involve decomposition of 1D surface brightness profiles and do not use a signal-to-noise weighting scheme as a result of the propensity for things to go awry at the centers of galaxies and consequentially wreak havoc on the fit. Differing from Savorgnan & Graham (2016), we have used the software packages from Ciambur (2015, 2016), which allowed us to better model the quasi-elliptical shape of the isophotes and perform more realistic PSF convolutions with our models.

3.2. Spitzer *Survey of Stellar Structure in Galaxies*

We have additionally compared our total apparent magnitudes to those from the *Spitzer* Survey of Stellar Structure in Galaxies (S^{4}G: Kim et al. 2014; Salo et al. 2015), which also examines an overlapping set of galaxies with our sample, and with identical imaging. In Figure 3, we find a low level of scatter of $\Delta_{rms,\perp} = 0.09$ mag with the six common galaxies from Kim et al. (2014) and $\Delta_{rms,\perp} = 0.06$ mag with the 14 common galaxies from Salo et al. (2015). These low levels of scatter are approximately one-half and one-fifth, respectively, of the scatter found among the spheroid apparent magnitudes for these same galaxies (see Paper I), and it is similar to the scatter found above from Savorgnan & Graham (2016).

Although we analyzed identical *Spitzer* images to the S^{4}G, they performed a 2D (opposed to our 1D) decomposition of the galaxies' observed surface brightness distributions. Kim et al. (2014) and Salo et al. (2015) utilized the BUDDA (de Souza et al. 2004; Gadotti 2008, 2009) and GALFIT (Peng et al. 2002, 2010) software routines, respectively. As Ciambur (2016) points out, pros and cons are associated with both 1D and 2D decomposition techniques. Neither approach is perfect, mainly as a result of some form of azimuthal averaging.

In particular, 1D codes work on azimuthally averaged isophotes, which collectively capture the radial gradients of the Fourier harmonic terms in these isophotes. Indeed, the discovery and measurement of the isophotal B_6 Fourier harmonic, as well as its association with (peanut shell)-shaped bulges, were made via 1D image analysis using ISOFIT (Ciambur 2015; Ciambur & Graham 2016). One of the advantages with collapsing a 2D image into a set of 1D profiles (e.g., surface brightness, ellipticity, position angle, and Fourier terms) is that the fitted galaxy model components, in one's subsequent decomposition of the light profile, account for these variations. That is, for example, one is not trying to fit a triaxial bulge with a 2D model that has a constant position angle and ellipticity, but rather one accounts for these isophotal twists and changes with radius. A fuller discussion can be found in Ciambur (2015, 2016).

[11] Throughout Paper I and this work, we analyze the agreement (in diagrams with the same quantity on both axes) by calculating the orthogonal rms scatter ($\Delta_{rms,\perp}$) about the 1:1 line, with $\Delta_{rms,\perp} = \Delta_{rms}/\sqrt{2}$.

4. Regression Analyses

Regression analysis in astronomy is simultaneously a crucial but inherently difficult task. Astronomical data are plagued with many complicating conditions arising from the difficulty of collecting data from great distances, selection effects, heteroscedasticity, etc. This complicates one's data sets, which ultimately must be compressed down to two numbers in a linear regression: slope and intercept. As a result, astronomers have developed many varied statistical approaches, manifest in the myriad of computer codes.

The astronomical community has been rapidly adopting Bayesian statistical methods over the past couple of decades (e.g., HyperFit, Pihajoki 2017. Andreon (2013) provide a review of measurement errors and scaling relations in astrophysics and advocate for Bayesian regression techniques. In deriving the $M_{\rm BH}$–$M_{*,\rm tot}$ and $M_{\rm BH}$–$M_{*,\rm disk}$ scaling relations in this paper, our custom Bayesian analysis (detailed in Paper I) explores both a conditional minimization of offsets in the vertical $\log M_{\rm BH}$ direction about the fitted line and a symmetric treatment of the data in both directions.

To date, many, if not most, of the published black hole mass scaling relations have been derived using either the BCES (Bivariate Correlated Errors and intrinsic Scatter; Akritas & Bershady 1996) or the MPFITEXY (Press et al. 1992; Tremaine et al. 2002; Bedregal et al. 2006; Novak et al. 2006; Markwardt 2009; Williams et al. 2010; Markwardt 2012) routine. For comparison, the data are additionally analyzed here using both of these more familiar routines. Reassuringly, when performing a "forward" regression (minimizing the vertical offset of the data about the fitted line), an "inverse" regression (minimizing the horizontal offset of the data about the fitted line), or instead treating the data symmetrically (here we use a line that bisects the slopes of the above two lines), we recover consistent scaling relations using each of these methods.

Ordinary least-squares regression bisection has been recommended for treating variables symmetrically for nearly three decades since the seminal work by Isobe et al. (1990). While our Bayesian analysis provides a symmetrical treatment of the (X, Y) data sets, as does the Akritas & Bershady (1996) routine, a symmetric treatment of the data can also be obtained when using the asymmetrical MPFITEXY routine by bisecting the results of the "forward" and "inverse" linear regressions (see, e.g., Novak et al. 2006). Although Graham & Li (2009) used BCES, MPFITEXY, and a different Bayesian code from Kelly (2007) and found that they all provided consistent results (see also Park et al. 2012, for a more detailed report), it remains prudent to check, especially as the BCES routine can struggle when the measurement errors are large (Tremaine et al. 2002). The recovery of slopes and intercepts that are consistent with each other will also provide confidence that one has not been led astray by a single statistical analysis.

The primary sources of uncertainty on the stellar mass estimates in our analyses consist of the individual uncertainties on the stellar mass-to-light ratios, distances, and photometry. The median relative uncertainties that we assigned to these terms in Paper I are 15%, 10%, and 10%, respectively.

4.1. Relations with Black Hole Mass (M_{BH})

4.1.1. The M_{BH}–$M_{*,tot}$ Relation

Our ($\log M_{*,\rm tot}$, $\log M_{\rm BH}$) data set has a Pearson correlation coefficient $r = 0.47$ and a p-value probability equal to 1.97×10^{-3} that the null hypothesis is true. The Spearman rank-order correlation coefficient $r_s = 0.53$, with $p_s = 4.53 \times 10^{-4}$ that the null hypothesis is true. We find the data to be slightly less correlated than the ($\log M_{*,\rm sph}$, $\log M_{\rm BH}$) data set we presented in Paper I, which had $r = 0.66$ with $p = 4.49 \times 10^{-6}$ and $r_s = 0.62$ with $p_s = 2.38 \times 10^{-5}$. Of course, one should bare in mind that the Pearson and Spearman correlation coefficients are ignorant of the error bars assigned to each data point. As such, one should turn to the uncertainty on the slope of the relation constructed through an analysis that allows for these errors. Our symmetric Bayesian analysis yields the following equation:

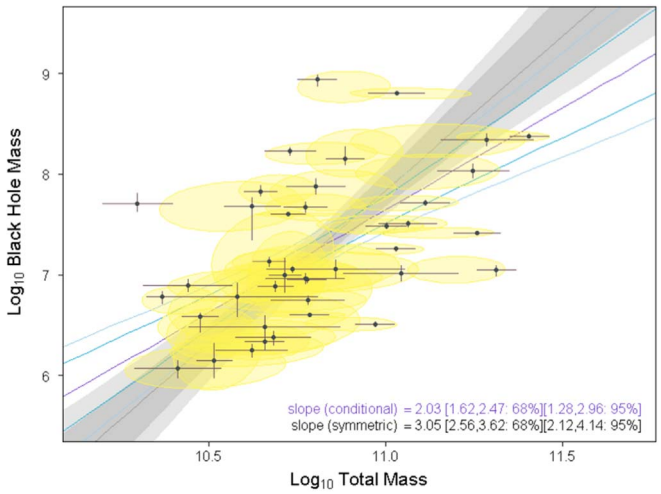

Figure 4. Symmetric (gray) Bayesian line of best fit (see Equation (3)) is presented as its pointwise median with ±68% and ±95% (shaded) intervals, while the ±68% posterior estimates of the true stellar total and black hole mass of each galaxy are highlighted in yellow. The conditional (purple) line of best fit is additionally supplied with similar (cyan) error intervals. Masses are in units of solar masses.

$$\log\left(\frac{M_{\rm BH}}{M_{\odot}}\right) = \left(3.05^{+0.57}_{-0.49}\right)\log\left[\frac{M_{*,\rm tot}}{\upsilon(6.37 \times 10^{10}\, M_{\odot})}\right] + \left(7.25^{+0.13}_{-0.14}\right), \quad (3)$$

with $\Delta_{\rm rms} = 0.79$ dex and $\epsilon = 0.69$ dex in the $\log M_{\rm BH}$ direction (see Figure 4). This regression, as well as all subsequent regressions in this work, is provided in Table 2. We note that the minimum vertical scatter is achieved when using the *conditional* regression, which yields $\Delta_{\rm rms} = 0.66$ dex and $\epsilon = 0.61$ dex.

In Figure 5, we present the data slightly differently than in Figure 4: we plot (but do not include in the regression)[12] the positions of the three excluded bulgeless galaxies from our sample and the bulgeless galaxy LEDA 87300 (Graham et al. 2016). Notably, our extrapolated MPFITEXY bisector linear regression coincides with the location of LEDA 87300, while NGC 4395 is an outlier.

4.1.2. The M_{BH}–$M_{*,disk}$ Relation

The ($\log M_{*,\rm disk}$, $\log M_{\rm BH}$) data set has $r = 0.28$, $p = 8.13 \times 10^{-2}$, $r_s = 0.34$, and $p_s = 3.06 \times 10^{-2}$. However, as noted

[12] If the three bulgeless spiral galaxies are included in the regression analysis, the BCES *bisector* routine finds a slope of 2.11 ± 0.37. This slope is only 69% as steep as the 40-galaxy slope; its shallowness is strongly influenced by the position of NGC 4395. Such a shallow slope is uncharacteristic, given that it is not steeper than the $M_{\rm BH}$–$M_{*,\rm sph}$ relation.

Table 2
Linear Regressions

Regression	Minimization	α	β	ϵ	$\Delta_{\rm rms}$	r	log$p$ (dex)	r_s	logp_s (dex)
(1)	(2)	(3)	(4)	(5)	(6)	(7)	(8)	(9)	(10)
40 Late-type Galaxies with Sérsic Bulges									
The $M_{\rm BH}$–$M_{*,\rm tot}$ Relation: $\log(M_{\rm BH}/M_\odot) = \alpha\log\{M_{*,\rm tot}/[\upsilon(6.37\times10^{10}\,M_\odot)]\} + \beta$									
Bayesian	*Symmetric*	$3.05^{+0.57}_{-0.49}$	$7.25^{+0.13}_{-0.14}$	0.69	0.79	0.47	−2.71	0.53	−3.34
Bayesian	$M_{\rm BH}$	$2.03^{+0.44}_{-0.41}$	$7.25^{+0.13}_{-0.14}$	0.61	0.66				
BCES	*Symmetric*	3.05 ± 0.70	7.25 ± 0.13	0.70	0.79				
BCES	$M_{\rm BH}$	2.04 ± 0.73	7.26 ± 0.11	0.61	0.66				
BCES	$M_{*,\rm tot}$	5.60 ± 1.57	7.25 ± 0.21	1.11	1.31				
MPFITEXY	*Symmetric*	2.65 ± 0.65	7.26 ± 0.14	0.65	0.73				
MPFITEXY	$M_{\rm BH}$	1.62 ± 0.39	7.27 ± 0.10	0.60	0.64				
MPFITEXY	$M_{*,\rm tot}$	5.94 ± 1.88	7.25 ± 0.23	1.18	1.39				
The $M_{\rm BH}$–$M_{*,\rm disk}$ Relation: $\log(M_{\rm BH}/M_\odot) = \alpha\log\{M_{*,\rm disk}/[\upsilon(4.98\times10^{10}\,M_\odot)]\} + \beta$									
Bayesian	*Symmetric*	$2.83^{+0.55}_{-0.42}$	7.24 ± 0.13	0.78	0.91	0.28	−1.09	0.34	−1.51
Bayesian	$M_{\rm BH}$	$1.74^{+0.43}_{-0.35}$	7.24 ± 0.13	0.67	0.75				
BCES	*Symmetric*	2.72 ± 1.07	7.30 ± 0.14	0.77	0.88				
BCES	$M_{\rm BH}$	1.48 ± 0.87	7.28 ± 0.12	0.66	0.72				
BCES	$M_{*,\rm disk}$	9.12 ± 4.70	7.41 ± 0.42	2.08	2.43				
MPFITEXY	*Symmetric*	2.38 ± 0.86	7.26 ± 0.17	0.73	0.83				
MPFITEXY	$M_{\rm BH}$	1.24 ± 0.39	7.26 ± 0.11	0.66	0.70				
MPFITEXY	$M_{*,\rm disk}$	8.53 ± 4.67	7.26 ± 0.37	1.94	2.28				
The $M_{*,tot}$–ϕ Relation: $\log(M_{*,\rm tot}/M_\odot) = \alpha[\lvert\phi\rvert - 13\overset{\circ}{.}4]\deg^{-1} + \beta + \log\upsilon$									
BCES	*Symmetric*	−0.053 ± 0.013	10.82 ± 0.04	0.20	0.25	−0.52	−3.29	−0.58	−4.04
BCES	$M_{*,\rm tot}$	−0.038 ± 0.008	10.82 ± 0.04	0.19	0.23				
BCES	$\lvert\phi\rvert$	−0.068 ± 0.024	10.83 ± 0.05	0.23	0.29				
MPFITEXY	*Symmetric*	−0.061 ± 0.013	10.80 ± 0.05	0.21	0.27				
MPFITEXY	$M_{*,\rm tot}$	−0.035 ± 0.009	10.81 ± 0.04	0.19	0.23				
MPFITEXY	$\lvert\phi\rvert$	−0.087 ± 0.018	10.79 ± 0.06	0.28	0.36				
The $M_{*,\rm disk}$–ϕ Relation: $\log(M_{*,\rm disk}/M_\odot) = \alpha[\lvert\phi\rvert - 13\overset{\circ}{.}4]\deg^{-1} + \beta + \log\upsilon$									
BCES	*Symmetric*	−0.054 ± 0.022	10.70 ± 0.05	0.24	0.30	−0.35	−1.61	−0.40	−1.99
BCES	$M_{*,\rm disk}$	−0.027 ± 0.010	10.69 ± 0.04	0.22	0.26				
BCES	$\lvert\phi\rvert$	−0.081 ± 0.043	10.70 ± 0.06	0.30	0.38				
MPFITEXY	*Symmetric*	−0.066 ± 0.018	10.70 ± 0.06	0.26	0.33				
MPFITEXY	$M_{*,\rm disk}$	−0.028 ± 0.010	10.70 ± 0.04	0.22	0.26				
MPFITEXY	$\lvert\phi\rvert$	−0.104 ± 0.026	10.69 ± 0.08	0.38	0.47				
21[a] Early-type Galaxies with Core-Sérsic Bulges									
The $M_{\rm BH}$–$M_{*,tot}$ Relation: $\log(M_{\rm BH}/M_\odot) = \alpha\log\{M_{*,\rm tot}/[\upsilon(2.58\times10^{11}\,M_\odot)]\} + \beta$									
BCES	*Symmetric*	1.34 ± 0.19	9.19 ± 0.09	0.37	0.40	0.68	−3.12	0.63	−2.66
BCES	$M_{\rm BH}$	0.96 ± 0.22	9.16 ± 0.10	0.34	0.38				
BCES	$M_{*,\rm tot}$	1.92 ± 0.43	9.25 ± 0.10	0.48	0.52				
MPFITEXY	*Symmetric*	1.32 ± 0.23	9.19 ± 0.07	0.37	0.40				
MPFITEXY	$M_{\rm BH}$	0.95 ± 0.25	9.15 ± 0.09	0.34	0.38				
MPFITEXY	$M_{*,\rm tot}$	1.90 ± 0.45	9.24 ± 0.12	0.48	0.52				

Note. Late-type galaxies are from this work, and early-type galaxies are from Savorgnan et al. (2016). The calculation of the total rms scatter ($\Delta_{\rm rms}$), the correlation coefficients (r and r_s), and their associated probabilities, do not take into account the uncertainties on the datapoints. Column (1): regression software used. Column (2): variable that had its offsets from the regression line minimized. Column (3): slope. Column (4): intercept. Column (5): intrinsic scatter in the vertical Y-coordinate direction (their Equation (1), Graham & Driver 2007). Column (6): total rms scatter in the Y-coordinate direction. Column (7): Pearson correlation coefficient. Column (8): logarithm of the Pearson correlation probability value. Column (9): Spearman rank-order correlation coefficient. Column (10): logarithm of the Spearman rank-order correlation probability value.

[a] This number was 22 in Savorgnan et al. (2016) because they considered NGC 4594 to have a core-Sérsic bulge (and not to be a spiral galaxy).

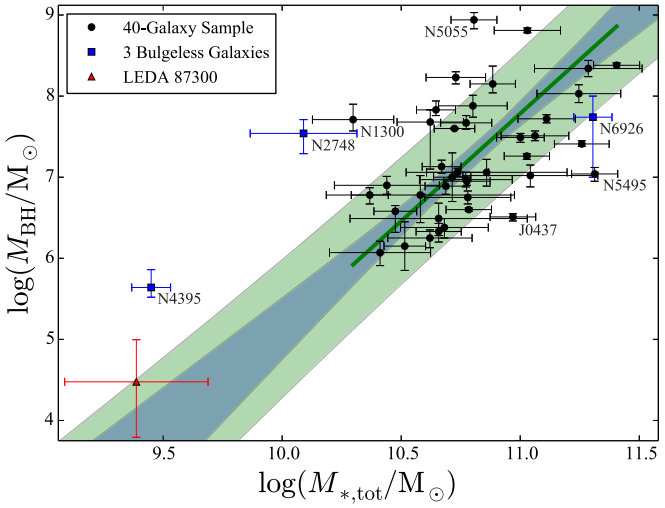

Figure 5. Similar to Figure 4, except here we also plot (but do not include in the regression) the three bulgeless galaxies from our sample and the bulgeless galaxy LEDA 87300 (Graham et al. 2016). Here, we plot the MPFITEXY bisector regression (solid green line). The dark-green band shows the $\pm 1\sigma$ uncertainty on the slope and the intercept from the regression, while the light-green band delineates the $\pm 1\sigma$ scatter of the data about the regression line.

before, this does not take into consideration the errors associated with the data points. Using the *symmetric* Bayesian analysis, we find

$$\log\left(\frac{M_{\rm BH}}{M_\odot}\right) = \left(2.83^{+0.55}_{-0.42}\right)\log\left[\frac{M_{*,\rm disk}}{\upsilon(4.98\times10^{10}\,M_\odot)}\right] + (7.24\pm0.13), \quad (4)$$

with $\Delta_{\rm rms} = 0.91$ dex and $\epsilon = 0.78$ dex in the log$M_{\rm BH}$ direction (see Figure 6). The conditional Bayesian analysis, which minimizes the offsets of the (error-weighted) data in the log$M_{\rm BH}$ direction, has $\Delta_{\rm rms} = 0.75$ dex and $\epsilon = 0.67$ dex (see Table 2).

In Figure 7, we plot (but do not include in the regression) the three bulgeless galaxies that were excluded from our sample, as well as the bulgeless galaxy LEDA 87300 (with masses taken from Graham et al. 2016). LEDA 87300 is consistent with the extrapolation of our MPFITEXY bisector linear regression to lower masses, while NGC 4395 is a slight outlier.

4.2. Relations with the Spiral Arm Pitch Angle (ϕ)

Nearly four decades ago, Kennicutt (1981) presented preliminary evidence that spiral arm pitch angle is correlated with $M_{*,\rm tot}$. Specifically, in his Figures 9 and 10, he illustrates a trend in both the ϕ–(absolute B-band galaxy magnitude) and the ϕ–(maximum rotational velocity) diagrams, respectively. With both of these quantities as indicators of total galaxy mass, it is not unexpected that we should recover a correlation between the pitch angle and the total stellar mass of a galaxy.

Since logarithmic spiral arm pitch angle (ϕ) has been shown to correlate well with black hole mass (Seigar et al. 2008; Berrier et al. 2013; Davis et al. 2017), it is prudent to check on the $M_{*,\rm tot}$–ϕ relation. We stress that the pitch angles are measured after first reprojecting the disks to a face-on orientation, and thus recovering the intrinsic geometry of the spiral arms. We additionally explore the possibility of a relation existing between $M_{*,\rm disk}$ and ϕ, given that the spiral pattern resides in the disk, and the bulk of a spiral galaxy's stellar mass is in its disk component.

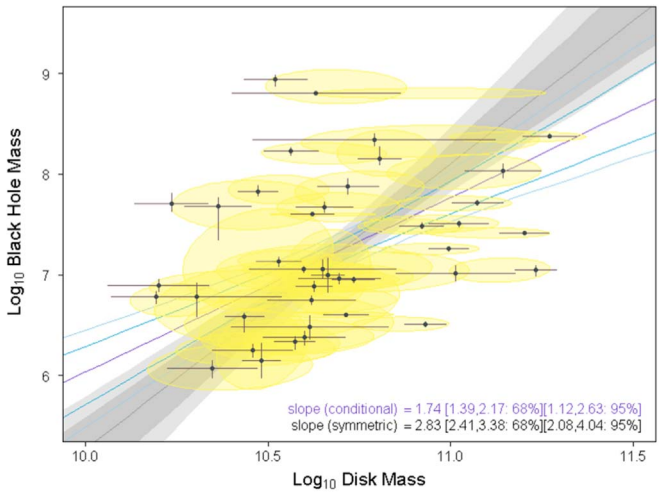

Figure 6. Similar to Figure 4, except that the disk stellar mass is plotted along the horizontal axis. The gray line is represented by Equation (4). Masses are in units of solar masses.

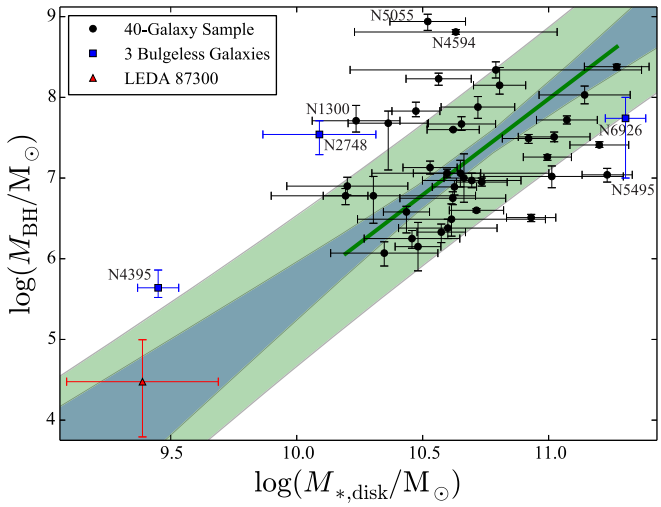

Figure 7. Similar to Figure 5, except that the stellar disk mass is plotted along the horizontal axis. Note that $M_{*,\rm disk} \equiv M_{*,\rm tot}$ for the bulgeless galaxies (including LEDA 87300) that are shown here, but they were excluded from the linear regression analysis (see Table 2).

We present the diagrams for the $M_{*,\rm tot}$–ϕ and $M_{*,\rm disk}$–ϕ relations in Figures 8 and 9, respectively, and the results are presented in Table 2. As was the case with the black hole mass relations, the stellar disk mass displays the weaker correlation among these two comparisons with pitch angle.

5. Discussion

5.1. From Bulge to Total Galaxy Mass

Läsker et al. (2014) reported agreement between their $M_{\rm BH}$–$L_{*,\rm sph}$ and $M_{\rm BH}$–$L_{*,\rm tot}$ relations, although their slopes are much shallower (both less than 1) than our slopes for the $M_{\rm BH}$–$M_{*,\rm sph}$ and $M_{\rm BH}$–$M_{*,\rm tot}$ relations (greater than 2 and 3, respectively) for spiral galaxies. However, their sample of 35 galaxies contained only four spiral galaxies and, as such, cannot so readily be compared to our analysis of 40 spiral galaxies. Läsker et al. (2014) also reported consistent intrinsic scatter between their $M_{\rm BH}$–$L_{*,\rm sph}$ and $M_{\rm BH}$–$L_{*,\rm tot}$ relations, whereas Savorgnan et al. (2016) found from their sample of 66

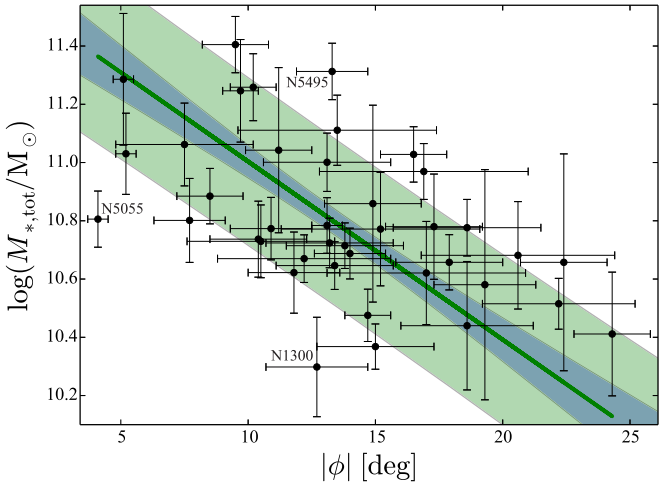

Figure 8. Logarithmic spiral arm pitch angle vs. the galaxy total stellar mass. The MPFITEXY bisector regression is presented (see Table 2).

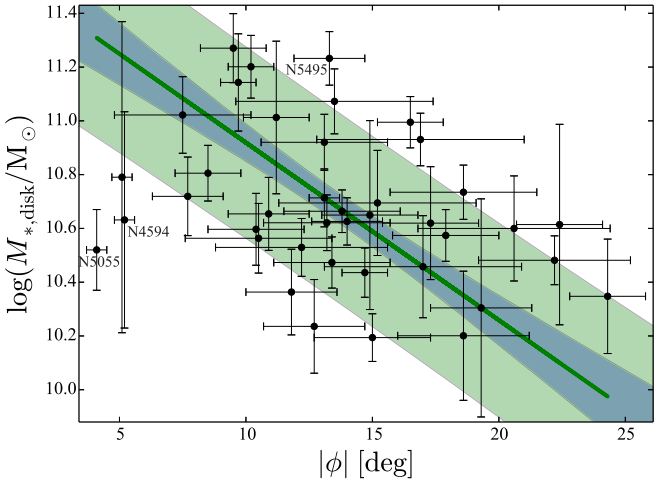

Figure 9. Logarithmic spiral arm pitch angle vs. the disk stellar mass. The MPFITEXY bisector regression is presented (see Table 2).

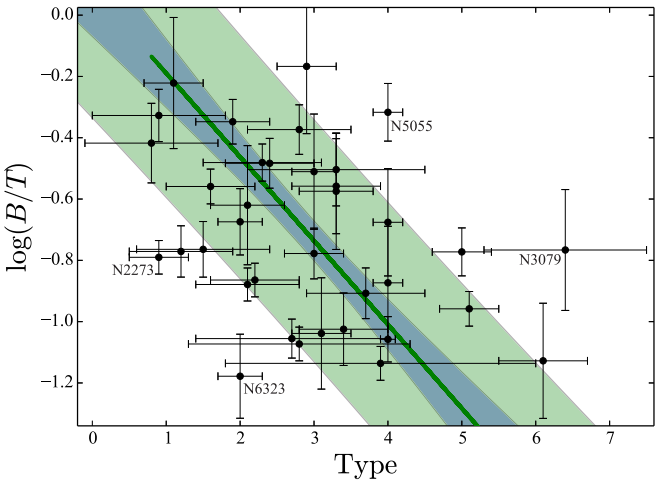

Figure 10. Logarithm of the bulge-to-total flux ratio vs. the numerical morphological type (for 36 spiral galaxies from our sample with both measurements), with Equation (5) plotted.

galaxies (including 17 spiral galaxies) that the claim of Läsker et al. (2014) is only valid for (bright) early-type galaxies. In N. Sahu et al. (2018, in preparation), we will provide the results from our analysis of ≈80 early-type galaxies with directly measured black hole masses, building on Läsker et al. (2014) and Savorgnan et al. (2016).

As for spiral galaxies with Sérsic bulges, when comparing the estimated intrinsic scatters from our various linear regressions, we find that the median intrinsic scatter for the M_{BH}–$M_{*,\mathrm{sph}}$ relation is 0.18 dex *less* than that of the M_{BH} –$M_{*,\mathrm{tot}}$ relation. Contrary to this, for a sample of 21 early-type galaxies with core-Sérsic bulges, taken from Savorgnan et al. (2016), we find that the median intrinsic scatter for the M_{BH}–$M_{*,\mathrm{sph}}$ relation is 0.05 dex more than that of the M_{BH}–$M_{*,\mathrm{tot}}$ relation. However, it should be borne in mind that the slope increases notably when going from the M_{BH}–$M_{*,\mathrm{sph}}$ to the M_{BH}–$M_{*,\mathrm{tot}}$ relation for late-type galaxies and roughly stays the same for early-type galaxies with core-Sérsic bulges. The increase of slope naturally causes the scatter to also increase in the vertical direction, i.e., along the black hole mass axis. This complicates the simple comparison of intrinsic scatter across scaling relations with various slopes.

We find a correlation between black hole mass and the total stellar mass of spiral galaxies that is not as strong ($r = 0.47$ and $r_s = 0.53$) as the correlation between black hole mass and bulge stellar mass ($r = 0.66$ and $r_s = 0.62$). The rms scatter in the $\log M_{\mathrm{BH}}$ direction from the *conditional* Bayesian linear regression, about the M_{BH}–$M_{*,\mathrm{tot}}$ relation, is 0.66 dex (cf. 0.60 dex for the M_{BH}–$M_{*,\mathrm{sph}}$ relation). The symmetric Bayesian analysis slope ($3.05^{+0.57}_{-0.49}$) is consistent with the BCES (3.05 ± 0.70) and MPFITEXY (2.65 ± 0.65) bisector slopes at the level of 0.00σ and 0.35σ, respectively. Likewise, the conditional Bayesian analysis slope ($2.03^{+0.44}_{-0.41}$) is consistent with the BCES (2.04 ± 0.73) and MPFITEXY (1.62 ± 0.39) ($Y \mid X$) slopes at the level of 0.01σ and 0.51σ, respectively.

Even though statistically equivalent (at the level of 0.73σ), the slope of our M_{BH}–$M_{*,\mathrm{tot}}$ relation (Equation (3)) is noticeably (25%) steeper than that of our M_{BH}–$M_{*,\mathrm{sph}}$ relation (Equation (12) Paper I). Because the bulge-to-total (B/T) flux ratio changes with the morphological type of spiral galaxies, as do the black hole masses, one does not expect M_{BH} versus T to have the same slope as M_{BH} versus B. In Figure 10, we explore this by first demonstrating that there indeed is a trend between the B/T flux ratio and the numerical morphological type; earlier types with more massive bulges have greater B/T ratios,[13] such that

$$\log\left(\frac{B}{T}\right) = -(0.27 \pm 0.08)[\mathrm{Type} - 2.85] - (0.70 \pm 0.06), \tag{5}$$

with $\Delta_{\mathrm{rms}} = 0.37$ dex and $\epsilon = 0.31$ dex in the $\log(B/T)$ direction from the BCES bisector regression; $r = -0.37$, $p = 2.73 \times 10^{-2}$, $r_s = -0.35$, and $p_s = 3.71 \times 10^{-2}$.

We additionally reveal how the B/T flux ratio changes with the black hole mass. In Figure 11, we show that the largest SMBHs (which typically reside in the largest bulges) have the largest $\log(B/T)$ values, thus confirming that the M_{BH}–$M_{*,\mathrm{tot}}$ relation should be steeper than the M_{BH}–$M_{*,\ \mathrm{sph}}$ relation. We

[13] This is consistent with the quantitative studies of Graham & Worley (2008) and largely driven by the changing bulge flux with spiral galaxy type (Yoshizawa & Wakamatsu 1975, their Figures 1 and 2).

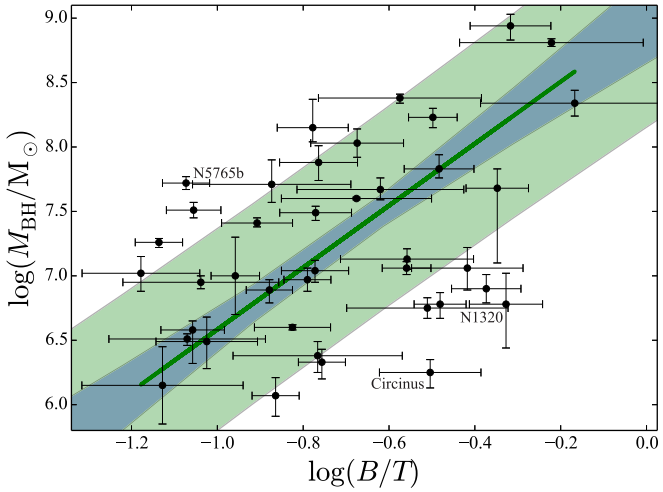

Figure 11. SMBH mass vs. the difference between the bulge and total flux, with Equation (6) plotted.

find from the BCES *bisector* analysis that

$$\log\left(\frac{M_{\rm BH}}{M_\odot}\right) = (2.41 \pm 0.46)\log\left[\frac{\log(B/T)}{-0.77}\right] + (7.15 \pm 0.12), \quad (6)$$

with $\Delta_{\rm rms} = 0.73$ dex and $\epsilon = 0.69$ dex in the $\log M_{\rm BH}$ direction; $r = 0.43$, $p = 5.43 \times 10^{-3}$, $r_s = 0.35$, and $p_s = 2.58 \times 10^{-2}$.

In Figure 12, we demonstrate that the $M_{\rm BH}$–$M_{*,\rm tot}$ relation has a steeper slope than the $M_{\rm BH}$–$M_{*,\rm sph}$ relation in Paper I, which can be understood via the morphological relations given above. Similarly, the $M_{*,\rm tot}$–ϕ relation (Figure 8 and Table 2) possesses a shallower slope than the $M_{*,\rm sph}$–ϕ relation (Paper I). The $M_{*,\rm tot}$–ϕ relation's shallowness is opposite to the $M_{\rm BH}$–$M_{*,\rm tot}$ relation's steepness because pitch angle is anticorrelated with black hole mass.[14] In passing, we note that we did explore the expected trend between black hole mass and galaxy color, but the overwhelming majority of spiral galaxies with directly measured black hole masses have red (B-K) colors, prohibiting the usefulness of this particular diagram at this stage.

Since our galaxies are disk dominated, the strong $M_{\rm BH}$–$M_{*,\rm sph}$ relation and weak $M_{\rm BH}$–$M_{*,\rm disk}$ relation suggest that the $M_{\rm BH}$–$M_{*,\rm tot}$ relation is governed mainly by the influence of the $M_{\rm BH}$–$M_{*,\rm sph}$ relation. While the latter relation may be more fundamental, the correlation between black hole mass and total galaxy stellar mass is probably more useful. It provides an easy and quick way to estimate central black hole mass in spiral galaxies by simply measuring the total luminosity and then converting into stellar mass.

Our presentation of the $M_{\rm BH}$–$M_{*,\rm disk}$ relation is primarily to demonstrate that black holes are not unrelated to properties of their galactic disks, which is partly reinforced by a strong correlation with the winding geometry of the spiral arms (which live in the disk). For late-type spiral galaxies, which have low bulge-to-disk (B/D) flux ratios compared to early-type spiral galaxies, the disk constitutes the majority of the total galaxy mass (see Figure 10). This implies that if the SMBH mass correlates with the total stellar mass—which need not be a direct correlation—then it should also correlate with the disk stellar mass. However, one can also appreciate how sample selection can result in one not finding this correlation: a small range of disk stellar masses, or a small number of galaxies, or poor disk magnitudes from the galaxy decomposition will hinder success.

[14] In the absence of uncertainty on $M_{\rm BH}$ or ϕ, the slopes for the various relations will be such that $M_{\rm BH}$–$M_{*,\rm sph} < M_{\rm BH}$–$M_{*,\rm tot} < M_{\rm BH}$–$M_{*,\rm disk}$ and $M_{*,\rm sph}$–$\phi > M_{*,\rm tot}$–$\phi > M_{*,\rm disk}$–ϕ. This can be seen by comparing the various *conditional* regressions that minimize the offsets with $M_{*,\rm sph}$, $M_{*,\rm tot}$, or $M_{*,\rm disk}$ from Paper I and this work.

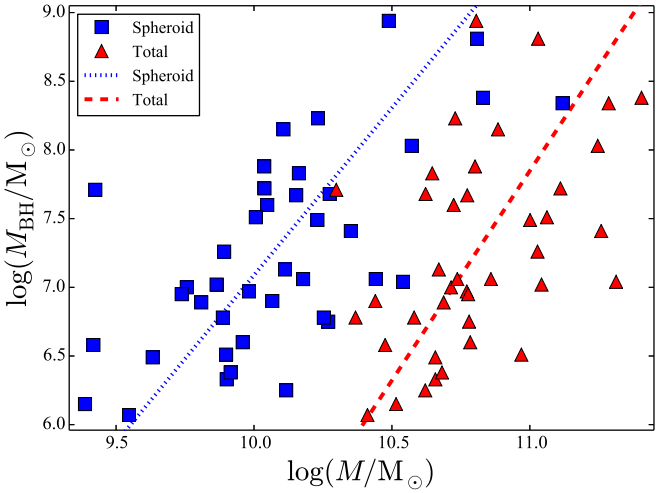

Figure 12. This figure combines the data from Figure 5 in Paper I with Figure 4 from this work, represented with blue and red, respectively. Shifting the total galaxy stellar masses (red triangles) left by an amount equal to $\log(B/T)$ transforms them into the spheroid stellar masses (blue squares). The dotted blue line and the dashed red line represent the symmetric Bayesian regression lines (Equation (12) from Paper I with Equation (3) from this work) for the spheroid and total stellar masses, respectively. Note that errors on individual points and on the fitted lines have been omitted for clarity.

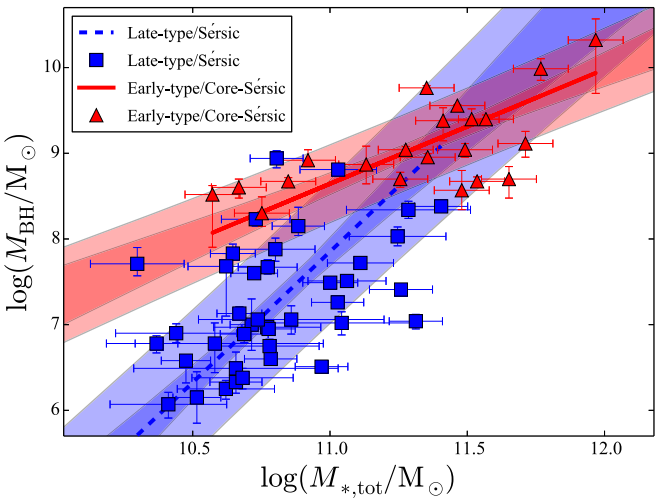

Figure 13. Comparison of $M_{\rm BH}$ vs. $M_{*,\rm tot}$ for our 40 late-type/Sérsic galaxies and 21 early-type/core-Sérsic galaxies from Savorgnan et al. (2016). Note that all trend lines are from the BCES bisector routine.

5.2. Potential Over/undermassive Black Holes

Figures 5 and 7 reveal that NGC 1300 and NGC 5055 are outliers above the $M_{\rm BH}$–$M_{*,\rm tot}$ and $M_{\rm BH}$–$M_{*,\rm disk}$ lines. Either their total/disk masses are lower than expected or their black hole masses are higher than expected. While NGC 5055 (also

known as M63 or the "Sunflower Galaxy") appears to have a slightly overmassive black hole in the $M_{\rm BH}$–$M_{*,\rm tot}$ and $M_{\rm BH}$–$M_{*,\rm disk}$ diagrams, it does not in the $M_{\rm BH}$–$M_{*,\rm sph}$ diagram in Paper I. However, Davis et al. (2017) revealed that NGC 5055 is a prominent outlier in the $M_{\rm BH}$–σ_* diagram (where σ_* is the stellar velocity dispersion), indicating a possible overmassive black hole in this galaxy. NGC 1300 stands out as a quintessential example of a strongly barred spiral galaxy with nuclear spiral arms; it is the least massive galaxy in our sample, yet its black hole appears to be overmassive by ≈1.5 dex. Finally, NGC 5495 is an outlier in most of the diagrams. Of our 40-galaxy sample, it has the second-highest $M_{*,\rm tot}$ and $M_{*,\rm disk}$. However, its black hole seems to be undermassive by ≈1.5 dex. NGC 1300 and NGC 5495 are outliers in all three relations: $M_{\rm BH}$–$M_{*,\rm sph}$, $M_{\rm BH}$–$M_{*,\rm tot}$, and $M_{\rm BH}$–$M_{*,\rm disk}$.

5.3. Relations with the Spiral Arm Pitch Angle (ϕ)

As with the $M_{\rm BH}$–$M_{*,\rm tot}$ relation (Figures 4 and 5), the $M_{*,\rm tot}$–ϕ relation (Figure 8) also displays a similarly correlated fit. Since our galaxies are mainly disk dominated (their median bulge-to-total flux ratio is 0.17), this implies that at least two properties of the disk (its stellar mass and pitch angle) should be correlated with the black hole mass. Furthermore, since the pitch angle correlates well with the SMBH mass (Seigar et al. 2008; Berrier et al. 2013; Davis et al. 2017) plus bulge mass and total mass (Figure 8 from Paper I and Figure 8 from this work), there should be a correlation between $M_{*,\rm disk}$ and ϕ, as demonstrated in Figure 9.

The strength of the correlation between $M_{*,\rm disk}$ and ϕ is less than that between $M_{*,\rm sph}$ and ϕ; the Pearson correlation coefficients are −0.35 and −0.63, respectively. This may seem unexpected, as the spiral arms are a feature of the disk. However, it should be remembered that the spiral density wave depends on the density of the disk, rather than the total mass of the disk, and it is the mass of the bulge that effectively anchors the spiral arm, a bit like setting the tension in the vibrating string of a violin by adjusting the tuning peg (Davis et al. 2015).

5.4. Morphology-dependent M_{BH}–$M_{*,tot}$ Relations

For comparison, we show (in Figure 13) how the $M_{\rm BH}$–$M_{*,\rm tot}$ relation appears when generated from a sample of early-type galaxies with core-Sérsic spheroids (which have black hole masses greater than $10^8\,M_\odot$)—thought to have been built from major dry merger events. We obtained measurements for a sample of 21 such galaxies from Savorgnan et al. (2016). By analyzing that sample separately from ours, we show that the slope for early-type core-Sérsic galaxies in the $M_{\rm BH}$–$M_{*,\rm tot}$ diagram (≈1.33) is half as steep as the slope of the $M_{\rm BH}$–$M_{*,\rm tot}$ relation for our 40 spiral galaxies (see Table 2).

Figure 13 shows a dichotomy between the slopes of early-type core-Sérsic galaxies and late-type Sérsic galaxies. If we compare the BCES *bisector* slopes of the $M_{\rm BH}$–$M_{*,\rm tot}$ relation for the early-type (1.34 ± 0.19) and late-type (3.05 ± 0.70) galaxies, we find that they are statistically different, agreeing only at the level of 1.92σ. This illustrates that the two samples are fundamentally different. Fitting a single power law to the combined sample yields a slope for the $M_{\rm BH}$–$M_{*,\rm tot}$ relation of 2.90 ± 0.21 (according to the BCES *bisector* routine). This is notably different from the slope of 1.71 ± 0.10 found in Paper I from fitting a single linear regression to the combined sample of 61 galaxies for the $M_{\rm BH}$–$M_{*,\rm sph}$ relation.

This clear difference in the relations between different morphological types echoes the results found in Savorgnan et al. (2016) and Paper I concerning the $M_{\rm BH}$–$M_{*,\rm sph}$ relation. In addition to these physical differences between samples of varying morphological types, important empirical ramifications exist for the study of black hole mass scaling relations. Therefore, we advise caution for studies of scaling relations concerning the demographics of one's chosen sample. This is not only true for local samples, where one needs to use the appropriate relation when predicting black hole masses, but care must also be given to evolutionary studies. For example, if one compared the $M_{\rm BH}$–$M_{*,\rm tot}$ relation from a local hybrid sample (of late- and early-type galaxies) with that from a higher-redshift galaxy sample of early-type galaxies, the scaling relations may differ solely as a result of the use of different morphological types at different epochs.

5.5. Predicting Black Hole Masses

Considering black hole mass scaling relations with ϕ, $M_{*,\rm sph}$, $M_{*,\rm tot}$, or σ_*, we advocate that ϕ be preferentially utilized for spiral galaxies with clear spiral structure. We say this based on the small total rms scatter, of just 0.43 dex in the $\log M_{\rm BH}$ direction, about the shallow $M_{\rm BH}$–ϕ relation (Davis et al. 2017). For spiral galaxies without clear spiral structure, $M_{*,\rm sph}$ should be utilized, depending on the desired accuracy and/or time requirements. For bulgeless spiral galaxies without clear spiral structure, $M_{*,\rm tot}$ can be used. Importantly, use of $M_{*,\rm tot}$ has the clear advantage that it can be measured for any spiral galaxy. In passing, we also note that the measurement of the stellar velocity dispersion σ_* requires telescope-time-expensive spectral data, while $M_{*,\rm sph}$ and $M_{*,\rm tot}$ just require photometric data, but ϕ needs only a photometrically uncalibrated image.

The rms scatter in the $\log M_{\rm BH}$ direction is 0.60 dex about the $M_{\rm BH}$–$M_{*,\ \rm sph}$ relation and 0.66 dex about the $M_{\rm BH}$–$M_{*,\ \rm tot}$ relation, each from the *conditional* Bayesian regressions. However, this quantity is not the "be all and end all" in deciding what relation is the most fundamental. It should be recognized that we have followed tradition and not advocated an error-weighted rms scatter, and as such, outlying data points with small measurement errors will inflate this reported scatter.

Finally, our newly defined relations allow us to estimate which galaxies might potentially harbor IMBHs ($10^2 \leqslant M_{\rm BH}/M_\odot \leqslant 10^5$). The *symmetric* Bayesian analyses[15] predict that galaxies with $M_{*,\rm tot} \leqslant \upsilon(1.16 \times 10^{10}\,M_\odot)$ and/or $M_{*,\rm disk} \leqslant \upsilon(8.05 \times 10^9\,M_\odot)$ should possess IMBHs.

In future work, we intend to explore the inclusion of additional parameters, which may potentially yield a tighter relation in the form of a 2D plane in a three-parameter space rather than a 1D line in a two-parameter space. The increased spatial resolution[16] and sensitivity[17] from the next generation of 20–30 m class telescopes will undoubtedly yield exciting results as one is afforded the ability to probe a little deeper into the

[15] It would be a mistake to extrapolate the *conditional* Bayesian line to masses below the mass range used to construct it, because its shallow slope would overestimate the black hole masses in this regime.

[16] Enables smaller spheres of influence to be measured.

[17] Provides less noisy spectra and therefore better velocity dispersions.

spiral galaxy (blue) sequence. Already, advancements with interferometry like the Atacama Large Millimeter/submillimeter Array (ALMA) are allowing one to achieve angular resolutions as small as 0.″02 (at 230 GHz with the 16 km baseline configuration).

An alternative avenue that we are currently pursuing is the use of X-ray emission to detect the presence of IMBHs in blue, late-type spiral galaxies (R. Soria et al. 2018, in preparation). Over 50 spiral galaxies in the Virgo Cluster have recently been observed with the Advanced CCD Imaging Spectrometer (ACIS-S) detector, as a part of the 559 ks *Chandra* Large Project titled "Spiral Galaxies of the Virgo Cluster" (PI: R. Soria; proposal ID: 18620568). We will use the $M_{\rm BH}$–$M_{*,\rm tot}$ relation from this paper, as well as the $M_{\rm BH}$–ϕ relation from Davis et al. (2017), to independently predict the black hole masses in these galaxies (Graham et al. 2018).

6. Conclusions

This work built on many recent studies of black hole mass scaling relations and has tried to advance the field by focusing on spiral galaxies with detailed bulge, disk, etc., decompositions. This has allowed us to better investigate the nature of the low-mass end of the black hole mass scaling relations with unparalleled accuracy and greatly narrow down the uncertainty on the slope of the $M_{\rm BH}$–$M_{*,\rm tot}$ relation for spiral galaxies. We find the following significant results:

1. As expected, the $M_{\rm BH}$–$M_{*,\rm tot}$ slope is steeper than the $M_{\rm BH}$–$M_{*,\rm sph}$ relation. We find $\log M_{\rm BH} \propto (3.05^{+0.57}_{-0.49}) \log M_{*,\rm tot}$, while Paper I found $\log M_{\rm BH} \propto (2.44^{+0.35}_{-0.31}) \log M_{*,\rm sph}$ for the same sample of 40 spiral galaxies.
2. For large surveys, where accurate bulge/disk decompositions may not be feasible, one may prefer to use the $M_{\rm BH}$–$M_{*,\rm tot}$ relation, with its slightly greater rms scatter of 0.79 dex (cf. 0.70 dex about the $M_{\rm BH}$–$M_{*,\rm sph}$ relation) in the $\log M_{\rm BH}$ direction when using the symmetric regression. The scatter reduces to 0.66 dex and 0.60 dex, respectively, when using the asymmetric (conditional) regression, which minimizes the scatter in only the $\log M_{\rm BH}$ direction.
3. It is advisable to not mix samples of early- and late-type galaxies. The slope of the $M_{\rm BH}$–$M_{*,\rm tot}$ relation for late-type galaxies is approximately twice as steep as that ($\approx$1.3) for early-type galaxies with core-Sérsic spheroids.
4. There *is* a relation between black hole mass and disk mass. Although the Spearman rank-order correlation coefficient is low, with $r_s = 0.34$ and $p_s = 3.06 \times 10^{-2}$, this does note take into account the uncertainties on the data points. Our symmetric Bayesian analysis reveals a well-defined relation (Equation (4)) with an $\approx$17% uncertainty on the slope. Furthermore, the low-mass bulgeless galaxy LEDA 87300 appears consistent with this relation at $M_{\rm BH} = 3.0 \times 10^4\, M_\odot$.
5. In Figures 8 and 9, we provide the relations between the spiral arm pitch angle (ϕ) and the stellar mass of the galaxy and disk (by which we include everything other than the bulge). Given the strong correlation between $M_{\rm BH}$ and ϕ (e.g., Davis et al. 2017), these two relations draw strong parallels with the two black hole mass scaling relations above. That is, we have checked and found consistency among these scaling relations.

Black hole mass scaling relations allow astronomers to quickly estimate black hole masses for large samples in an era of astrophysics research that is dominated by massive amounts of data. We present a refined $M_{\rm BH}$–$M_{*,\rm tot}$ relation for spiral galaxies, which is capable of producing expeditious, yet accurate, SMBH mass predictions.

We thank Nandini Sahu for her helpful comments and insights, which helped improve this paper. A.W.G. was supported under the Australian Research Council's funding scheme DP17012923. Parts of this research were conducted by the Australian Research Council Centre of Excellence for Gravitational Wave Discovery (OzGrav), through project no. CE170100004. This research has made use of NASA's Astrophysics Data System. This research has made use of the NASA/IPAC Infrared Science Archive. We acknowledge the usage of the HyperLeda database (Makarov et al. 2014), http://leda.univ-lyon1.fr. This research has made use of the NASA/IPAC Extragalactic Database (NED). Some of the data presented in this paper were obtained from the Mikulski Archive for Space Telescopes (MAST). This publication makes use of data products from the Two Micron All Sky Survey, which is a joint project of the University of Massachusetts and the Infrared Processing and Analysis Center/California Institute of Technology. The BCES routine (Akritas & Bershady 1996) was run via the PYTHON module written by Rodrigo Nemmen (Nemmen et al. 2012), which is available at https://github.com/rsnemmen/BCES. Error propagation calculations were performed via the PYTHON package, UNCERTAINTIES (http://pythonhosted.org/uncertainties/).

Appendix A
Propagation of Uncertainty

Here, we provide formulae necessary to calculate uncertainties on properties of the disk and total galaxy. For the complementary equations for properties of the spheroid, see Equations (7) and (10) from Paper I.

$$\mathfrak{m}_{\rm disk} = -2.5 \log (10^{-0.4\mathfrak{m}_{\rm tot}} - 10^{-0.4\mathfrak{m}_{\rm sph}}) \tag{7}$$

$$\delta\mathfrak{m}_{\rm disk} = \frac{\sqrt{(L_{\rm tot}\,\delta\mathfrak{m}_{\rm tot})^2 + (L_{\rm sph}\,\delta\mathfrak{m}_{\rm sph})^2}}{L_{\rm tot} - L_{\rm sph}} \tag{8}$$

$$\delta\mathfrak{M}_{\rm tot} = \sqrt{\delta\mathfrak{m}_{\rm tot}^2 + \left[\frac{5(\delta d_L)}{d_L \ln(10)}\right]^2} \tag{9}$$

$$\delta\mathfrak{M}_{\rm disk} = \sqrt{\frac{(L_{\rm tot}\,\delta\mathfrak{m}_{\rm tot})^2 + (L_{\rm sph}\,\delta\mathfrak{m}_{\rm sph})^2}{(L_{\rm tot} - L_{\rm sph})^2} + \left[\frac{5(\delta d_L)}{d_L \ln(10)}\right]^2} \tag{10}$$

$$\delta \log M_{*,\rm tot} = \sqrt{\left(\frac{\delta\mathfrak{m}_{\rm tot}}{2.5}\right)^2 + \left[\frac{2(\delta d_L)}{d_L \ln(10)}\right]^2 + \left[\frac{\delta\Upsilon_*}{\Upsilon_* \ln(10)}\right]^2} \tag{11}$$

$$\delta \log M_{*,\rm disk} = \sqrt{\frac{(L_{\rm tot}\,\delta\mathfrak{m}_{\rm tot})^2 + (L_{\rm sph}\,\delta\mathfrak{m}_{\rm sph})^2}{[2.5(L_{\rm tot} - L_{\rm sph})]^2} + \left[\frac{2(\delta d_L)}{d_L \ln(10)}\right]^2 + \left[\frac{\delta\Upsilon_*}{\Upsilon_* \ln(10)}\right]^2} \tag{12}$$

Table 3
Fitting Results of Our Model against the Observational Data Set ($\log M_{*,\rm tot}$, $\log M_{\rm BH}$)

	Prior					Posterior				
Quantile	2.5%	16%	50%	84%	97.5%	2.5%	16%	50%	84%	97.5%
Symmetric slope	0.03	0.19	1.00	5.30	39.35	2.12	2.56	3.05	3.62	4.14
Conditional ($Y \mid X$) slope	0.02	0.17	0.90	4.77	36.12	1.28	1.62	2.03	2.47	2.96
Symmetric $M_{\rm BH}$ scatter (dex)	0.01	0.05	0.22	0.68	1.65	0.63	0.70	0.79	0.90	1.00
Conditional $M_{\rm BH}$ scatter (dex)	0.01	0.05	0.21	0.67	1.61	0.45	0.51	0.58	0.66	0.75
Normalized X-intercept, X_0	6.58	8.51	10.50	12.49	14.42	10.71	10.76	10.80	10.85	10.90
Normalized Y-intercept, Y_0	3.08	5.01	7.00	8.99	10.92	6.98	7.11	7.25	7.38	7.52

Table 4
Fitting Results of Our Model against the Observational Data Set ($\log M_{*,\rm disk}$, $\log M_{\rm BH}$)

	Prior					Posterior				
Quantile	2.5%	16%	50%	84%	97.5%	2.5%	16%	50%	84%	97.5%
Symmetric slope	0.03	0.19	0.99	5.27	39.79	2.08	2.41	2.83	3.38	4.04
Conditional ($Y \mid X$) slope	0.02	0.17	0.92	4.74	34.78	1.12	1.39	1.74	2.17	2.63
Symmetric $M_{\rm BH}$ scatter (dex)	0.01	0.05	0.21	0.68	1.56	0.64	0.71	0.80	0.90	1.04
Conditional $M_{\rm BH}$ scatter (dex)	0.01	0.05	0.22	0.68	1.57	0.49	0.55	0.62	0.70	0.81
Normalized X-intercept, X_0	6.58	8.51	10.50	12.49	14.42	10.60	10.65	10.70	10.75	10.80
Normalized Y-intercept, Y_0	3.08	5.01	7.00	8.99	10.92	6.98	7.11	7.24	7.37	7.50

Appendix B
Bayesian Prior and Posterior Values

Here, we summarize the results of fitting our Bayesian models against the observational data sets of the $M_{\rm BH}$–$M_{*,\rm tot}$ (Table 3) and $M_{\rm BH}$–$M_{*,\rm disk}$ (Table 4) relations. In particular, we report the estimated quantiles at 2.5%, 16%, 50%, 84%, and 97.5% for each parameter; from these can be read the median, 68% ("$\pm1\sigma$"), and 95% ("$\pm2\sigma$") credible intervals. Illustrations of our fits are also presented in Figures 4 and 6. From inspection of Tables 3 and 4, it is evident that our priors are strongly updated by the data.

ORCID iDs

Benjamin L. Davis https://orcid.org/0000-0002-4306-5950
Alister W. Graham https://orcid.org/0000-0002-6496-9414

References

Akritas, M. G., & Bershady, M. A. 1996, ApJ, 470, 706
Andreon, S., & Hurn, M. 2013, Statistical Analysis and Data Mining: The ASA Data Science Journal, 9, 15
Baldassare, V. F., Reines, A. E., Gallo, E., & Greene, J. E. 2015, ApJL, 809, L14
Bedregal, A. G., Aragón-Salamanca, A., & Merrifield, M. R. 2006, MNRAS, 373, 1125
Beifiori, A., Courteau, S., Corsini, E. M., & Zhu, Y. 2012, MNRAS, 419, 2497
Bell, E. F., & de Jong, R. S. 2001, ApJ, 550, 212
Bell, E. F., McIntosh, D. H., Katz, N., & Weinberg, M. D. 2003, ApJS, 149, 289
Bennert, V. N., Auger, M. W., Treu, T., Woo, J.-H., & Malkan, M. A. 2011, ApJ, 742, 107
Bennert, V. N., Treu, T., Woo, J.-H., et al. 2010, ApJ, 708, 1507
Berrier, J. C., Davis, B. L., Kennefick, D., et al. 2013, ApJ, 769, 132
Burkert, A., Förster Schreiber, N. M., Genzel, R., et al. 2016, ApJ, 826, 214
Cassata, P., Guzzo, L., Franceschini, A., et al. 2007, ApJS, 172, 270
Chabrier, G. 2003, PASP, 115, 763
Chilingarian, I. V., & Zolotukhin, I. Y. 2012, MNRAS, 419, 1727
Ciambur, B. C. 2015, ApJ, 810, 120
Ciambur, B. C. 2016, PASA, 33, e062
Ciambur, B. C., & Graham, A. W. 2016, MNRAS, 459, 1276
Cisternas, M., Jahnke, K., Bongiorno, A., et al. 2011, ApJL, 741, L11
Combes, F. 2009, in ASP Conf. Ser. 419, Galaxy Evolution: Emerging Insights and Future Challenges, ed. S. Jogee et al. (San Francisco, CA: ASP), 31
Combes, F. 2017, in SF2A-2017: Proc. Annual Meeting of the French Society of Astronomy and Astrophysics, ed. C. Reylé et al. (Paris), 223
Combes, F., & Sanders, R. H. 1981, A&A, 96, 164
Contini, T., Epinat, B., Bouché, N., et al. 2016, A&A, 591, A49
Davis, B. L., Graham, A. W., & Cameron, E. 2018, arXiv:1810.04887
Davis, B. L., Graham, A. W., & Seigar, M. S. 2017, MNRAS, 471, 2187
Davis, B. L., Kennefick, D., Kennefick, J., et al. 2015, ApJL, 802, L13
de Souza, R. E., Gadotti, D. A., & dos Anjos, S. 2004, ApJS, 153, 411
de Vaucouleurs, G., de Vaucouleurs, A., Corwin, H. G., Jr., et al. 1991, Third Reference Catalogue of Bright Galaxies
den Brok, M., Seth, A. C., Barth, A. J., et al. 2015, ApJ, 809, 101
Dressler, A. 1989, in IAU Symp. 134, Active Galactic Nuclei, ed. D. E. Osterbrock & J. S. Miller (Dordrecht: Kluwer), 217
Ferrarese, L. 2002, ApJ, 578, 90
Gadotti, D. A. 2008, MNRAS, 384, 420
Gadotti, D. A. 2009, MNRAS, 393, 1531
Graham, A. W. 2012, ApJ, 746, 113
Graham, A. W. 2016, in Astrophysics and Space Science Library, Vol. 418, Galactic Bulges, ed. E. Laurikainen, R. Peletier, & D. Gadotti (Switzerland: Springer), 263
Graham, A. W., Ciambur, B. C., & Soria, R. 2016, ApJ, 818, 172
Graham, A. W., & Driver, S. P. 2007, ApJ, 655, 77
Graham, A. W., & Li, I.-h. 2009, ApJ, 698, 812
Graham, A. W., & Scott, N. 2013, ApJ, 764, 151
Graham, A. W., Soria, R., & Davis, B. L. 2018, MNRAS, submitted
Graham, A. W., & Worley, C. C. 2008, MNRAS, 388, 1708
Hopkins, P. F., Hernquist, L., Cox, T. J., & Kereš, D. 2008, ApJS, 175, 356
Isobe, T., Feigelson, E. D., Akritas, M. G., & Babu, G. J. 1990, ApJ, 364, 104
Jahnke, K., Bongiorno, A., Brusa, M., et al. 2009, ApJL, 706, L215
Jahnke, K., & Macciò, A. V. 2011, ApJ, 734, 92
Jarrett, T. H., Chester, T., Cutri, R., et al. 2000, AJ, 119, 2498
Kelly, B. C. 2007, ApJ, 665, 1489
Kennicutt, R. C., Jr. 1981, AJ, 86, 1847
Kim, T., Gadotti, D. A., Sheth, K., et al. 2014, ApJ, 782, 64
Kollmeier, J. A., Onken, C. A., Kochanek, C. S., et al. 2006, ApJ, 648, 128
Kormendy, J., & Gebhardt, K. 2001, in AIP Conf. Ser. 586, 20th Texas Symp. on Relativistic Astrophysics, ed. J. C. Wheeler & H. Martel (Melville, NY: AIP), 363

Labbé, I., Rudnick, G., Franx, M., et al. 2003, ApJL, 591, L95
Läsker, R., Ferrarese, L., van de Ven, G., & Shankar, F. 2014, ApJ, 780, 70
Licquia, T. C., & Newman, J. A. 2015, ApJ, 806, 96
Makarov, D., Prugniel, P., Terekhova, N., Courtois, H., & Vauglin, I. 2014, A&A, 570, A13
Markwardt, C. 2012, MPFIT: Robust Non-linear Least Squares Curve Fitting, Astrophysics Source Code Library, ascl:1208.019
Markwardt, C. B. 2009, in ASP Conf. Ser. 411, Astronomical Data Analysis Software and Systems XVIII, ed. D. A. Bohlender, D. Durand, & P. Dowler (San Francisco, CA: ASP), 251
Masters, K. L., Mosleh, M., Romer, A. K., et al. 2010, MNRAS, 405, 783
Meidt, S. E., Schinnerer, E., van de Ven, G., et al. 2014, ApJ, 788, 144
Merloni, A., Bongiorno, A., Bolzonella, M., et al. 2010, ApJ, 708, 137
Mutlu-Pakdil, B., Seigar, M. S., Hewitt, I. B., et al. 2018, MNRAS, 474, 2594
Nemmen, R. S., Georganopoulos, M., Guiriec, S., et al. 2012, Sci, 338, 1445
Novak, G. S., Faber, S. M., & Dekel, A. 2006, ApJ, 637, 96
Okamoto, T. 2013, MNRAS, 428, 718
Oke, J. B. 1974, ApJS, 27, 21
Park, D., Kelly, B. C., Woo, J.-H., & Treu, T. 2012, ApJS, 203, 6
Peng, C. Y. 2007, ApJ, 671, 1098
Peng, C. Y., Ho, L. C., Impey, C. D., & Rix, H.-W. 2002, AJ, 124, 266
Peng, C. Y., Ho, L. C., Impey, C. D., & Rix, H.-W. 2010, AJ, 139, 2097
Pihajoki, P. 2017, MNRAS, 472, 3407
Press, W. H., Teukolsky, S. A., Vetterling, W. T., & Flannery, B. P. 1992, Numerical Recipes in FORTRAN. The Art of Scientific Computing (2nd ed.; Cambridge: Cambridge Univ. Press)
Querejeta, M., Meidt, S. E., Schinnerer, E., et al. 2015, ApJS, 219, 5
Robotham, A. S. G., & Obreschkow, D. 2015, PASA, 32, e033
Roediger, J. C., & Courteau, S. 2015, MNRAS, 452, 3209
Salo, H., Laurikainen, E., Laine, J., et al. 2015, ApJS, 219, 4
Savorgnan, G. A. D., & Graham, A. W. 2016, ApJS, 222, 10
Savorgnan, G. A. D., Graham, A. W., Marconi, A., & Sani, E. 2016, ApJ, 817, 21
Schlafly, E. F., & Finkbeiner, D. P. 2011, ApJ, 737, 103
Scott, N., Graham, A. W., & Schombert, J. 2013, ApJ, 768, 76
Seigar, M. S., Kennefick, D., Kennefick, J., & Lacy, C. H. S. 2008, ApJL, 678, L93
Shankar, F., Weinberg, D. H., & Miralda-Escudé, J. 2009, ApJ, 690, 20
Sheth, K., Regan, M., Hinz, J. L., et al. 2010, PASP, 122, 1397
Taylor, E. N., Hopkins, A. M., Baldry, I. K., et al. 2011, MNRAS, 418, 1587
Tremaine, S., Gebhardt, K., Bender, R., et al. 2002, ApJ, 574, 740
Volonteri, M., Natarajan, P., & Gültekin, K. 2011, ApJ, 737, 50
Walter, F., Banados, E., Venemans, B., et al. 2016, AAS Meeting 227, 243.39
Williams, M. J., Bureau, M., & Cappellari, M. 2010, MNRAS, 409, 1330
Yang, G., Brandt, W. N., Vito, F., et al. 2018, MNRAS, 475, 1887
Yoshizawa, M., & Wakamatsu, K. 1975, A&A, 44, 363
Yuan, T., Richard, J., Gupta, A., et al. 2017, ApJ, 850, 61
Zhao, W., Braatz, J. A., Condon, J. J., et al. 2018, ApJ, 854, 124